Elsevier Editorial System(tm) for Journal of Hazardous Materials
Manuscript Draft

Manuscript Number: HAZMAT-D-09-04731

Title: Field rates for natural attenuation of arsenic in Tinto Santa Rosa Acid Mine Drainage (SW Spain)

Article Type: Research Paper

Keywords: Keywords: arsenic, oxidation, sorption, modelling, acid mine drainage

Corresponding Author: Mrs Maria P. Asta,

Corresponding Author's Institution: Zaragoza University

First Author: Maria P. Asta

Order of Authors: Maria P. Asta; Carlos Ayora; Patricia Acero; Jordi Cama

Abstract: Reactive transport modelling of the main processes related to the arsenic natural attenuation observed in the Acid Mine Drainage (AMD) impacted stream of Tinto Santa Rosa (SW, Spain) was performed. Despite the simplicity of the kinetic expressions used to deal with arsenic attenuation processes, the model reproduced succesfully the major chemical trends observed along the acid discharge. Results indicated that the rate of ferrous iron oxidation was similar to the one obtained in earlier field studies in which microbial catalysis is reported to occur. With regard to the scaled arsenic oxidation rate, it is one order of magnitude faster than the values obtained under laboratory conditions suggesting the existence of a catalytic agent in the natural system. As regards the schwertmannite precipitation rate, which was represented by a simple kinetic expression relying on Fe(III) and pH, was in the range calculated for other AMD impacted sites. Finally, the obtained distribution coefficients used for representing arsenic sorption onto Fe(III) precipitates were lower than those deduced from reported laboratory data. This discrepancy is attributed to a decrease in the schwertmannite arsenate sorption capacity as sulphate increases in the solution.

Department of Earth Sciences,
Zaragoza University
María P. Asta

Zaragoza, 11/27/2009

To whom it may concern

Dear Sir or Madam,

Please find submitted our paper entitled:

"Field rates for natural attenuation of arsenic in Tinto Santa Rosa Acid Mine Drainage (SW Spain)"

María P. Asta [(1)*], Carlos Ayora [(1)], Patricia Acero [(2)] and Jordi Cama [(1)]

[(1)] Institute of Environmental Assessment and Water Research (IDAEA), CSIC, C/Jordi Girona, 18-26, 08034 Barcelona, Spain

[(2)] Petrology and Geochemistry Area, Earth Sciences Department, C/Pedro Cerbuna 12, 50009 Zaragoza, Spain

*Corresponding author: mpasta@unizar.es; present address: Petrology and Geochemistry Area, Earth Sciences Department, C/Pedro Cerbuna 12, 50009 Zaragoza, Spain

phone #: 34+976761000 ext. 3159

fax #: +34 976 761106

This manuscript is an original work; it was not published elsewhere and is not under consideration for publication elsewhere.

All authors have seen the manuscript and agree to its submission to *Journal of Hazardous Materials*

In this paper a 1D reactive transport model coupling advective flux and the main geochemical processes controlling arsenic mobility in AMD systems is proposed. The model is useful to evaluate and quantify the relative influence of those processes on the arsenic fate along an AMD discharge and to explore the effects of reaction rate scaling to field conditions. In addition, this study allow understanding the arsenic attenuation processes and the improvement and management of AMD systems.

Thank you in advance,

Yours faithfully,

María Pilar Asta

*Manuscript
Click here to view linked References

Field rates for natural attenuation of arsenic in Tinto Santa Rosa Acid Mine Drainage (SW Spain)

María P. Asta[(1)*], Carlos Ayora[(1)], Patricia Acero[(2)] and Jordi Cama[(1)]

[(1)] Institute of Environmental Assessment and Water Research (IDAEA), CSIC, C/Jordi Girona, 18-26, 08034 Barcelona, Spain

[(2)] Petrology and Geochemistry Area, Earth Sciences Department, C/Pedro Cerbuna 12, 50009 Zaragoza, Spain

*Corresponding author: mpasta@unizar.es. Present address: Petrology and Geochemistry Area, Earth Sciences Department, C/Pedro Cerbuna 12, 50009 Zaragoza, Spain

phone #: 34+976761000 ext. 3159

fax #: +34 976 761106

Abstract

Reactive transport modelling of the main processes related to the arsenic natural attenuation observed in the Acid Mine Drainage (AMD) impacted stream of Tinto Santa Rosa (SW, Spain) was performed. Despite the simplicity of the kinetic expressions used to deal with arsenic attenuation processes, the model reproduced succesfully the major chemical trends observed along the acid discharge. Results indicated that the rate of ferrous iron oxidation was similar to the one obtained in earlier field studies in which microbial catalysis is reported to occur. With regard to the scaled arsenic oxidation rate, it is one order of magnitude faster than the values obtained under laboratory conditions suggesting the existence of a catalytic agent in the natural system. As regards the schwertmannite precipitation rate, which was represented by a simple kinetic expression relying on Fe(III) and pH, was in the range calculated for other AMD impacted sites. Finally, the obtained distribution coefficients used for representing arsenic sorption onto Fe(III) precipitates were lower than those deduced from reported laboratory data. This discrepancy is attributed to a decrease in the schwertmannite arsenate sorption capacity as sulphate increases in the solution.

Keywords: arsenic, oxidation, sorption, modelling, acid mine drainage

1 Introduction

Acid mine drainage (AMD), generated by sulphide oxidative dissolution, may lead to high concentrations of dissolved metals and metalloids, including arsenic. Given its importance, much research has been aimed at characterizing the arsenic sources in mining areas, the mechanisms controlling arsenic release and mobility and its natural attenuation [1]. These studies have led to the identification and description of the main geochemical processes that control the mobility and fate of arsenic in surface and ground waters. A group of studies have also focused on the complex interrelationships and couplings among these processes [2-6].

Even though many of the cited processes are strongly dependent on the hydrogeological processes present in each system, only a few recent works, have approached them with the assistance of reactive transport modelling [7-9]. Reactive transport modelling is an essential tool for the quantitative evaluation of arsenic in the environment because the location and rate of reactions are controlled by both chemistry and transport. Such quantitative models are indispensable to plan efficient remediation strategies and to predict the evolution of water quality in rivers and reservoirs.

In line with this, one of the main problems encountered during the implementation of reactive transport models is related to the choice of the rates for the involved geochemical processes. One possible approach to this problem consists in using laboratory experimental reaction rates and rate laws. However, the poorly-known scaling of such rates to adapt them to field sites represents a serious drawback to this

approach. Therefore, it is of paramount importance to obtain quantitative sets of field data to determine the reaction rates and rate laws for the processes involved in the metal(loid)s transport and attenuation.

For these purposes, the waters and mineral precipitates from the acid discharge of the Tinto Santa Rosa abandoned mine (Iberian Pyritic Belt (IPB), SW Spain) were thoroughly studied and a 1D-reactive transport model, coupling advective flux and the main geochemical processes controlling arsenic mobility, was developed. This stream was chosen because of the simplicity of its flow system, and because its hydrogeochemical and mineralogical features are generally similar to many acid mine drainage streams not only in the Iberian Pyritic Belt [10-12] but also in other acid drainages world-wide [13-15]. The implementation of the reactive transport model applied to this thoroughly-characterized natural system allowed evaluating the relative influence of the many geochemical processes on the arsenic fate along a representative AMD-discharge and exploring the scaling of reaction rates to field conditions.

2 Materials and Methods

2.1-Field site and sampling description

All the water and sediment samples described in this study were collected in March of 2007 and February of 2008 along the acid discharge (Fig. 1). The stream flows in a narrow channel (1.5-2 m wide) over different terrace levels of yellowish and reddish loose and crusty precipitates.

At each of the sampling points, pH, temperature, Eh and conductivity were measured in situ and three water subsamples were taken in acid-pre-washed polyethylene bottles, after rinsing thoroughly with filtered local water. Two of the subsamples were filtered through a 0.1-μm pore membrane filter. One of these subsamples was acidified with HNO_3 for elemental analyses and the other was acidified with HCl, adjusting its pH to less than 1, for dissolved Fe(II)/Fe(III) determination. The third water subsample, for arsenic speciation determination, was preserved following the method of Oliveira et al. [16] for AMD samples. It consists of eluting the sample through a column filled with a cationic exchange resin that reduces the load of metals that can act as potential oxidizing agents but without affecting the arsenic species. All the water samples were preserved in the dark at 4ºC until analyzed. Fe(II)/Fe(III) and As(III)/As(V) were determined in less than 48 h since sampling.

2.2-Analytical methods

Water pH was measured in the field using a Crison® glass electrode with automated temperature compensation after calibration with standard buffer solutions of pH 2 and 7. Redox potential was measured using a Pt combination electrode (ThermoOrion SureFlow®) checked against solutions of 220 and 468 mV. The measurements were corrected to the Standard Hydrogen Electrode (SHE). Electrical conductivity was measured with a Pt cell calibrated with KCl 0.1 and 0.01 m solutions. The measurement errors for pH, Eh and conductivity were ≤ 0.05 pH units, ≤ 5 mV and ±1%, respectively.

Concentrations of major elements in solution were measured by Inductively Coupled Plasma Atomic Emission Spectrometry (ICP-AES) using a Perkin-Elmer® Optima 3200

65 RL. Detection limits were 0.1 mg L^{-1} for Al, Si and S; 0.05 mg L^{-1} for Ca, Mg, 0.5 mg L^{-1}
66 for K, 0.025 mg L^{-1} for Fe, Zn, Cu and Mn and 2 mg L^{-1} for Na. The error was estimated
67 to be below 3%. Concentrations of trace metals (Ni, Cd, Co, As, Pb, Sb, Ti and V) were
68 analyzed by Inductively coupled plasma mass spectroscopy (ICP-MS) using a Perkin-
69 Elmer® Sciex Elan 6000 instrument. Detection limits were on the order of 1 μg L^{-1} and
70 the error was estimated to be below 5%.

71 Ferrous and total dissolved iron concentrations were determined by colourimetry
72 using the ferrozine method [17] in a UV–VIS HP Spectrophotometer. Fe(III) was taken
73 as the difference between Fe(tot) and Fe(II). The quality of the results was assured by
74 measuring several standards, blanks and duplicates. Fe(tot) concentrations matched
75 ICP-AES results within 10%.

76 Arsenic speciation from the AMD water samples was obtained by High Performance
77 Liquid Chromatography- Inductively Coupled Plasma Mass Spectroscopy (HPLC-ICP-
78 MS). The microHPLC system consisted of an Agilent 1100 Series (Agilent, Waldbronn,
79 Germany) binary pump and auto injector with a programmable sample loop (20 μL
80 maximum). The separations were performed on a PRP-X100 (Hamilton, Reno, NV,
81 USA) anion exchange column (100 mm × 1 mm, 7 μm i.d.) and a phosphate buffer
82 (H_3PO_4 12 mM,) as a mobile phase (pH 3) at a flow rate of 80 μL min^{-1}. The microbore
83 column was connected directly to a Micromist nebulizer and a high-efficiency
84 nebulizer (HEN) using its own capillary (480 mm × 0.25 mm and 480 mm × 0.10 mm,
85 respectively). An HP 4500 ICP-MS instrument (Yokogawa Analytical Systems, Tokyo,
86 Japan) was used for the determinations. Detection limit for the arsenic species was <
87 0.05 μg L^{-1}. Concentrations matched ICP-MS results within 15%.

3 Geochemical characterisation of the Tinto Santa Rosa AMD system

The water flow measured in 2007 and 2008 campaigns was 0.7 and 1.1 L s^{-1}, respectively. About 2/3 of the water comes from the mouth an aerated adit and has large concentrations of Fe and sulphate, with a noticeable content of minor elements (TS1 in Table 1). Seven meters downstream, the stream receives a groundwater discharge probably connected with flooded galleries (TS2 in Table 1) and that contains higher concentrations of arsenic and lead and larger proportions of As(III) than the water coming from the adit mouth. No water sources other than the mine drainage (TS1 and TS2) were observed: the bed is made up of low permeability schists, and no lateral tributaries are present. Downstream from these points, the pH decreases, which is accompanied by a systematic decrease of ferrous and total iron concentrations. These changes can be reasonably attributed to the Fe(II) oxidation to Fe(III) and its subsequent precipitation as ferric oxy-hydroxy-sulphates.

The evolution along the stream of some major dissolved elements (Na, Mg, Ca, Al, and SO_4) shows a constant concentration (Table 1) due to their low reactivity during transport in aquatic systems at the measured pH range. Moreover, the constant concentration of these elements downstream points out that no important evaporation takes place, and confirms the absence of other water sources that could cause dilution.

Whereas the concentrations of other dissolved minor elements do not change significantly downstream (Cd and Sr) or decrease only slightly (Ni, Cu, Pb and Zn), the concentrations of total arsenic decreased sharply downstream (Table 1). This clear

decrease in dissolved arsenic concentrations is accompanied by a decrease of As(V) concentrations and, especially, of As(III) contents (Table 1). Since no other inflows were detected, this behaviour can be attributed to the oxidation of As(III) to As(V), which presents a stronger affinity than As(III) for Fe(III)-precipitates [18-19] within the measured pH range and is partially sorbed onto them. The quantification and assessment of all these processes will be performed in the following sections.

Iron precipitates are extensively described in Asta et al. [20]. Mineralogically, the solid phases collected in the stream bed consist of schwertmannite, goethite and jarosite. Schwertmannite, with ideal formula $Fe_8O_8(OH)_{5.5}(SO_4)_{1.25}$, is the dominant secondary phase although its proportion decreases downstream, accompanied by an increase in goethite and jarosite. The most concentrated element amongst the minor elements analyzed in the solids is arsenic (Table 2), which decreases downstream mirroring its behaviour in the stream water concentration. Whereas upstream this element is mainly linked to schwertmannite, downstream it appears also associated to goethite and jarosite [20]. The contents of the rest of elements (Zn, Cd, Ni, Sb, V and Co but, especially, Mn, Cu and Pb) in the iron precipitates are also significant.

4 Model description

4.1. Conceptual model

The conceptual model of arsenic mobilization and attenuation includes the following processes: (1) Fe(II) oxidation to Fe(III); (2) oxidation of As(III) to As(V); (3) Fe(III)

precipitation as oxy-hydroxy-sulphates, causing a pH decrease; and (4) sorption of As(V) onto the solid Fe(III)-phases. The global overall reactions representing these processes are shown in Table 3 (eq. 1 to 4).

The rate of Fe(II) oxidation was implemented in the model by using the expression of Singer and Stumm [21] for pH below 3.5:

$$r_{Fe(II)} = \frac{-d[Fe(II)]}{dt} = k_{Fe}[Fe(II)]\ f_{O_2} \quad (1)$$

where $r_{Fe(II)}$ is the oxidation rate expressed in mol L^{-1} s^{-1}, [Fe(II)] is the ferrous iron concentration (mol L^{-1}) at a time t (s), fO_2 is the oxygen fugacity and k_{Fe} (s^{-1}) is the rate constant of the kinetic expression. This reaction is known to be very slow at low pH [21] except in the presence of microorganisms, which increase the rate of Fe(III) production by up to six orders of magnitude.

As(III) commonly oxidizes to As(V) but this reaction is known to proceed very slowly [22-23]. However, the rate of oxidation of As(III) to As(V) by Fe(III) is increased by several orders of magnitude by the presence of near-ultraviolet light because the reaction (eq. 2; Table 3) takes place in conjunction with the photochemical reduction of Fe(III) [24]. Moreover, As(III) oxidation to As(V) is assumed to be catalyzed by the biotically-oxidized Fe(III) and, therefore, microbially-mediated redox processes affecting iron and arsenic seem to be coupled. In order to take into account this coupling, the following equation is proposed:

$$r_{As(III)} = \frac{-d[As(III)]}{dt} = k_{As}\ [As(III)]\ [Fe(III)] \quad (2)$$

where k_{As} is an oxidation coefficient (L mol^{-1} s^{-1}), calibrated against the field data; and [As(III)] and [Fe(III)] are the arsenite and ferric iron concentrations, respectively (in mol L^{-1}).

The oxidation of As(III) to As(V) plays a central role in arsenic attenuation, since the ferric precipitates that cover the stream bed (mainly schwertmannite, goethite and jarosite) show a capacity to sorb As(V) larger than As(III) under the acidic pH conditions observed in the system. The usual ferric phase directly precipitated in many sites of the IPB is schwertmannite [25, 26]. The precipitation of goethite and jarosite in low-temperature systems is known to be very slow [27] (weeks to months at room temperature). Therefore, although goethite and jarosite are present in the studied site, these phases are considered to have formed by recrystallization of schwertmannite. The schwertmannite ageing and transformation to goethite and/or jarosite may also last some months [25], and it is still delayed by the presence of large amounts of sorbed arsenate [13]. Given that the water residence time estimated in the stream is only of a few hours, we reasonably assume that ferric iron removal from water between the mixing point and TS8 (Fig.1) is due to schwertmannite precipitation.

As regards the rate of schwertmannite precipitation, no experimental rates of schwertmannite precipitation have been found in the literature, although it is reasonable to assume that this rate is proportional to supersaturation (see for example, Molson et al., [9]):

$$r_{Sch} = k_{Sch} (\Omega - 1) \quad (3)$$

where Ω is the schwertmannite saturation, defined as the ratio of the ion activity product and the solubility product, and k_{Sch} is the rate constant (mol L^{-1} s^{-1}). However, this expression introduces a high variability in the deduced rate constant values even though this process was apparently constant in the field. This is due to the high stoichiometric coefficients of the ions in the schwertmannite precipitation reaction (Table 3). Thus, small variations in an ion concentration cause high variations in the ion activity product. In addition to that, several solubility products with differences in orders of magnitude, have been proposed for schwertmannite [28, 29]. Therefore, a simple kinetic expression that relies on empirical concentrations was used:

$$r_{Sch} = k_{Sch} [Fe(III)] [H^+]^{-1} \quad (4)$$

where r_{Sch} is the rate of schwertmannite precipitation (in mol L^{-1} s^{-1}); [Fe(III)] and [H^+] are the ferric iron concentration (in mol L^{-1}) and proton activity, respectively; and k_{Sch} is the rate constant (in mol L^{-1} s^{-1}). It is worth noting that the used expression is qualitatively similar to that of equation 3, since the sulphate concentration is almost conservative (it can be integrated in the k_{Sch} value).

The last process included in the model was the arsenic decrease due to As(V) sorption onto schwertmannite. This Fe(III)-oxyhydroxysulphate is a reputed sink for As(V) in AMD due to sorption processes [13, 30]. Sorption of As(V) can occur through true adsorption (or surface complexation) or through co-precipitation. Both As(V) uptake mechanisms seem to consist of the replacement of SO_4 groups by AsO_4 [13, 30, 31]. In the Tinto Santa Rosa model, the As(V) sorption rate has been assumed to depend mainly on the following three factors: (1) the availability of schwertmannite (i.e.

189 schwertmannite precipitation rate); (2) the concentration of As(V); and (3) a
190 distribution coefficient characteristic of the sorption/co-precipitation process.
191 Therefore, the following simple kinetic expression, combining the effects of these three
192 processes, was included in the model:

$$r_{As(V)} = r_{Sch}\, k_d [As(V)] \quad (5)$$

193 where $r_{As(V)}$ is the As(V) sorption rate (mol L^{-1} s^{-1}); r_{Sch} is the schwertmannite
194 precipitation rate (mol L^{-1} s^{-1}), as calculated by eq. 3; [As(V)] is the arsenate
195 concentration in mol L^{-1} and k_d represents the partition coefficient for As(V) into
196 schwertmannite.

197 4.2 Reactive transport model implementation

198 The one dimensional (1D) reaction-transport model was carried out with the assistance
199 of the PHREEQC code [32] and using the WATEQ4F thermodynamic database [33]. In
200 the simulations, a 1D path 300 m long and divided into 20 equal cells was used. A flow
201 rate of 0.7 and 1.1 L s^{-1} was considered, according to the rate measurements carried out
202 in March 2007 and in February 2008, respectively. The distances between the different
203 sampling points, located by GPS in the field, were calculated by means of ArcGIS 9
204 over the aerial orthoimage of the Tinto Santa Rosa stream. The travelling time between
205 points was estimated with the flow rate and the stream section measured in the field.

206 Model inputs included measured temperature, pH, pE and elemental concentrations.
207 The water composition that resulted from the mixing water of the two contaminant

208 sources (TS1 and TS2 from Table 1 in a mixing ratio of 0.7TS1/0.3TS2) was used as the
209 initial water composition.

210 5 Results and discussion

211 Figures 2 and 3 display the measured pH and the dissolved concentrations of total
212 iron, Fe(II), Fe(III), total arsenic, As(III) and As(V) along the Tinto Santa Rosa stream,
213 together with the results obtained in the simulations for the same type of data.

214 The rate of Fe(II) oxidation was calculated from the decrease in the Fe(II) concentration
215 between the TS1 - TS2 mixing point and point TS8 (Fig. 1). The residence time of water
216 estimated between these points was 3.2 and 2.1 h, depending on the flow rate of the
217 corresponding campaign. The resulting Fe(II)-oxidation field rate ranged from $3.4x10^{-7}$
218 mol L^{-1} s^{-1} to $4.3x10^{-7}$ mol L^{-1} s^{-1}. These rates are roughly 5 orders of magnitude higher
219 than the abiotic laboratory value of $3.0x10^{-12}$ mol L^{-1} s^{-1}, proposed by Singer and Stumm
220 [34], which is clearly attributable to the catalyzing effect of bacteria under field
221 conditions. The corresponding rate constant values for Fe(II) oxidation are of $10^{-3.55}$ and
222 $10^{-3.75}$ L mol^{-1} s^{-1}. These kinetic constant values are only slightly higher than those
223 obtained by using the same first-order kinetic expression for biotic experiments carried
224 out under laboratory conditions ($10^{-4.1}$ to $10^{-5.2}$ L mol^{-1} s^{-1}; unpublished data). Moreover,
225 the rate constants for the Tinto Santa Rosa system are very similar to the values
226 obtained in earlier field works [35, 36], which adds robustness to the model and
227 parameters used for Fe(II) oxidation in streams. After fixing the oxidation rates of Fe(II)
228 and As(III), Fe(III) precipitation rates were fitted. As done for Fe(II), the As(III)
229 oxidation rate at the field scale was calculated taking into account the decrease in

As(III) concentration from TS1-TS2 to TS8 and the residence time required (Figure 3). The obtained oxidation rate constant is $10^{-1.2}$ L mol^{-1} s^{-1}, which is around one order of magnitude faster than the one obtained in the laboratory under atmospheric conditions (from $10^{-2.2}$ to $10^{-2.8}$ L mol^{-1} s^{-1}, unpublished data). As explained above, As(III) may be oxidised by Fe(III) in the presence of light (eq. 2 in Table 3) and this oxidation path is considerably faster than that promoted only by dissolved oxygen. Therefore, the higher As(III) oxidation rate observed in the field is attributed to the catalytic effect exerted by ferric iron and solar light, although some biocatalytic influence cannot be ruled out. Nonetheless, a marked decrease in the As(III) dissolved concentration on February 2008 is observed in the upper reaches of the stream (between TS1-TS2 mixing point and TS3) and it is not totally reproduced by the model (Fig. 3c). This discrepancy might be attributed to diel differences in solar irradiation during sampling, since ultraviolet light induces rapid photooxidation of As(III) to As(V) [37]. Another possible explanation is that high Fe(II)/Fe(III) ratios (as observed upstream) increase the production of hydroxyl radicals, therefore increasing the oxidation rate of As(III). However, the obtained data do not allow confirming or discarding any of these hypotheses, which should certainly be addressed in the future.

The Fe(III)-removal rate owing to schwertmannite precipitation was calculated from the differences in the Fe(III)-concentration along the stream (eq. 3; Table 3). The estimated schwertmannite precipitation rate was of $3.1x10^{-7}$ and $1.7x10^{-7}$ mol L^{-1} s^{-1} for the data of March 2007 and February 2008, respectively. These rate values are in the range of $1.7x10^{-6}$ to 10^{-7} mol L^{-1} s^{-1} reported by Sánchez-España et al. [26] using the

252 differences of total dissolved iron for other AMD impacted sites in the Iberian Pyritic
253 Belt (IPB).

254 The model reproduces reasonably the field data from the two sampling campaigns
255 with precipitation rate constant values of $10^{-8.0}$ and $10^{-8.5}$ mol L^{-1} s^{-1} (k_{Sch} in eq. 4 above),.
256 As a test of the significance of these values and given the absence of similar
257 precipitation expressions in the literature, our kinetic expression was used to model the
258 data reported by Acero et al. [25] for the Cueva de la Mora stream, which is located
259 also in the Iberian Pyritic Belt. A precipitation constant of $10^{-8.1}$ mol L^{-1} s^{-1} was obtained
260 by coupling Fe(II)-oxidation (with an oxidation rate constant of $10^{-3.65}$ L mol^{-1} s^{-1}, in the
261 range proposed here for the Tinto Santa Rosa system) and schwertmannite
262 precipitation, which is in good agreement with the precipitation rate constant obtained
263 in the Tinto Santa Rosa AMD.

264 The fitting between the simulated and measured pH values was used as an
265 independent check of the model implemented to reproduce the observed iron
266 concentration evolution in the Tinto Santa Rosa system. The observed evolution trend
267 of pH is known to be mainly controlled by the iron geochemistry in AMD systems.
268 Iron removal from the dissolved phase demands the oxidation of ferrous iron followed
269 by hydrolysis of ferric iron and precipitation as ferric oxy-hydroxy-sulphate mineral
270 phases. All these processes have a clear influence on pH evolution; Fe(II) oxidation
271 consumes hydrogen ions whereas ferric iron precipitation releases protons. Thus, the
272 balance between the consumption and release of hydrogen ions is the main pH-
273 determining control in this type of systems. As displayed in Figure 2, the measured pH
274 was suitably fitted by the reactive transport model without any additional calibration.

Therefore, this is an independent evidence supporting the significance of the obtained rates for Fe(II) oxidation and schwertmannite precipitation and the general soundness of the developed model.

Finally, the arsenic uptake processes by precipitating ferric phases were incorporated to the model by means of distribution coefficients representing the partitioning of arsenic between aqueous and solid phases owing to both potential adsorption and co-precipitation in association with schwertmannite. Kinetic sorption of As(V) onto schwertmannite was modelled by incorporating As(V) as a minor constituent into precipitated schwertmannite (eq. 4; Table 3). Distribution coefficients of $10^{3.42}$ and $10^{3.90}$ adequately predict the evolution of the measured As(V) concentration. These values are lower than the coefficients that can be deduced from the laboratory data obtained by Fukushi et al. [30] using similar As(V) concentrations (distribution coefficients between $10^{4.5}$ and $10^{5.0}$). Since arsenic sorption onto schwertmannite is though to occur via sulphate-arsenate exchange [31], the large sulphate concentrations in the Tinto Santa Rosa stream (from 2800 to 3500 mg L^{-1}), much higher than in their laboratory experiments (10-70 mg L^{-1}), could be the cause of the lower uptake of arsenic observed in our case.

As can also be observed in Figure 3, the predicted arsenic evolution slightly overestimates the field values in the lower reaches of the acid stream. This is possibly due to the fact that only schwertmannite has been included as a precipitating ferric phase in the model whereas also goethite and jarosite, with notably different arsenic uptake capacities [38], are present (especially in those lower stream reaches).

6 Sensitivity analysis

In the following section, the sensitivity of model results as well as the uncertainties associated with the major processes and the values of key parameters in the calibrated model are tested with the 2008 data set.

The impact of uncertainty in the Fe(II)-oxidation rate constant (k_{Fe}) was tested by increasing and decreasing the rate constant by one order of magnitude. The increase of the $k_{Fe(II)}$ leads to a pH increase since the oxidation process consumes protons (Fig. 4). Nevertheless, the expected increase in pH is mitigated to an extent by increasing the schwertmannite precipitation rate. Despite this attenuation due to the precipitation, $k_{Fe(II)}$ values higher than $10^{-3.4}$ led to an anomalous pH increase in the upper stream reaches. This pH increase, not observed under field conditions, occurred as a result of the predominance of the oxidation processes (which consume protons) over precipitation (which generates protons). As expected, high oxidation rates also leads to lower Fe(II) and higher Fe(III) contents in the simulations than those observed in the field (Fig. 5a,b). According to the sensitivity results, a experimentally supported range for the Fe(II) oxidation rate constant is $10^{-3.7\pm0.2}$ for the Tinto Santa Rosa stream.

The influence of the arsenite oxidation rate constant (k_{As}) in the calculations was tested by increasing and decreasing the rate constant by one order of magnitude (Fig. 6). The results of the simulations showed that very high arsenite oxidation rates led not only to As(III) concentrations much lower than measured in the stream but also to an anomalous increase in the As(V) contents in the upper part of the stream, which was not observed in the field. On the other hand, as expected, lower oxidation rate

constants led to higher As(III) concentrations in the simulations than in the field data. According to the results, As(III) is more sensible than As(V) to variations in the oxidation rate constants (Fig. 6). Despite the poor agreement between the modelled and experimental points of this particular data set, the model adequately predicted the experimental points of 2007 data set. Acceptable values for the oxidation rate constants are those ranged from $10^{-1.2\pm0.2}$.

As stated above, the changes in the pH value due to Fe(II) oxidation were mitigated by the Fe(III) precipitation that produces protons. According to the simulation results, the main process that affects the pH value is the schwertmannite precipitation, as it was expected since the process generates around 20 moles of protons for each mol of schwertmannite precipitated (Fig. 7a). Experimentally supported values for the precipitation constant are ranged within $10^{-8.4\pm0.2}$ (Fig. 7a,b).

The sensitivity of the model to the arsenic distribution coefficient (k_d in eq. 5 above) was checked by increasing and decreasing its value between $10^{3.6}$ and $10^{4.5}$ ($10^{4.5}$ corresponds to the distribution coefficient calculated from the Fukushi et al. [30]). As expected, the use of larger distribution coefficients results in higher sorption capacities of the bed-stream solids and, therefore, leads to lower As(V) concentrations than observed under field conditions (Fig. 8). On the contrary, the use of smaller distribution coefficients produces As(V) concentrations higher in the simulations than in the field. The experimentally supported range for this distribution coefficient is $10^{3.95\pm0.1}$.

7 Conclusions

A 1-D reactive transport model coupling advective flux and several chemical reactions has proved to be useful in predicting the geochemical behaviour of an AMD stream. A remarkable innovation in this model is the incorporation of key chemical reactions such as iron and arsenic oxidation, precipitation of schwertmannite and arsenic sorption onto the newly precipitated schwertmannite on the stream bed.

Our geochemical modelling highlights the importance of iron oxidation, which ultimately controls the geochemical changes observed in the system. On the one hand, Fe(III) is capable of oxidizing As(III) and, on the other hand, the precipitation of Fe(III) phases plays a key role as a sink for As(V) due to sorption.

Despite the simplicity of the model, the simulations satisfactorily reproduced the main chemical features of the stream water, such as the pH decrease downstream and the accompanying changes in As(III), As(V), Fe(II), and Fe(III) concentrations. The fitted kinetic constants for iron oxidation are comparable to those reported in earlier studies using similar rate law expressions under field and laboratory biotic conditions.

The model calibration demonstrated the need for scaling the arsenic oxidation rate obtained under laboratory conditions in order to reproduce real field rates, which have shown to be up to one order of magnitude faster. The reason is not clear from our work, but it could be due to the effect of biocatalysts, Fe(III) and/or solar light in As(III) oxidation. The same need for field scaling has been proven for the arsenate distribution coefficient onto schwertmannite, which have been observed to be lower than calculated

from data obtained under laboratory conditions. This is probably due to the fact that the effectiveness of the schwertmannite sorption mechanism, which was suggested in earlier studies to occur via sulphate-arsenate exchange, is likely diminished by the presence of high sulphate concentrations.

Finally, a schwertmannite precipitation rate law, calibrated to reproduce the iron evolution, has been used in the model and applied to reproduce successfully not only the data from the two sampling campains presented in this study but also the trends observed at another independent AMD site in the Iberian Pyritic Belt.

In light of the sensitivity analysis results, it can be concluded that the calculations are very sensitive to the used rate constants and, therefore, the values obtained for these factors are meaningful.

8 Acknowledgements

This research was funded by the project CTM2007-66724-C02-01/TECNO from the Spanish Government. MPA was financially supported by the Spanish Government with a PhD fellowship. PA was financially supported by the Spanish Government with a research contract from the "Juan de la Cierva" program. We are also indebted to M. Caraballo, A.M. Sarmiento, C. Torrentó and J.M. Nieto for their help during the field campaign and to V. Ouro and A. Roig for analytical assistance. We are grateful to J.M. Soler for his helpful comments during the preparation of the manuscript.

9 References

[1] H. Cheng, Y. Hu, J. Luo, B. Xu, J. Zhao, Geochemical processes controlling fate and transport of arsenic in acid mine drainage (AMD) and natural systems, J. Hazard. Mater. 165 (2008) 13-26.

[2] O. Sracek, P. Bhattacharya, G. Jacks, J.P. Gustafsson, M. Von Brömssen, Behavior of arsenic and geochemical modeling of arsenic enrichment in aqueous environments, Appl. Geochem. 19 (2004) 269-180.

[3] K.G. Stollenwerk, G.N. Breit, A.H. Welch, J.C. Yount, J.W. Whitney, A.L. Foster, M.N. Uddin, R.K. Majumder, N. Ahmed, Arsenic attenuation by oxidized aquifer sediments in Bangladesh, Sci. Total Environ. 379 (2007) 133-150.

[4] M.U. Sharif, R.K. Davis, K.F. Steele, B. Kim, T.M. Kresse, J.A. Fazio, Inverse geochemical modeling of groundwater evolution with emphasis on arsenic in the Mississippi River Valley alluvial aquifer, Arkansas (USA), J. Hydrol. 350 (2008) 41-55.

[5] G. Cornelis, S. Poppe, T. Van Germen, E. Van den Broeck, M. Ceulemans, C. Vandecasteele, Geochemical modelling of arsenic and selenium leaching in alkaline water treatment sludge from the production of non-ferrous metals, J. Hazard. Mater. 159 (2008) 271-279.

[6] P.G. Whitehead, D. Butterfield, A.J. Wade, Simulating metals and mine discharges in river basins using a new INtegrated CAtchment model for metals: pollution impacts and restoration strategies in the aries-mures river system in Transylvania, Romania, Hydrol. Res. 40 (2009) 323-346.

[7] R.L. Runkel, B.A. Kimball, Reactive solute transport in streams: a surface complexation approach for trace metal sorption, Water Resour. Res. 35 (1999) 3829-3840.

[8] C. Le Guern, P. Baranger, C. Crouzet, F. Bodénan, P. Conil, Arsenic trapping by iron oxyhydroxides and carbonates at hydrothermal spring outlets, Appl. Geochem. 18 (2003) 1313-1323.

[9] J. Molson, M. Aubertin, B. Bussière, M. Benzaazoua, Geochemical transport modelling of drainage from experimental mine tailings cells covered by capillary barriers, Appl. Geochem. 23 (2008) 1-24.

[10] J. Sánchez-España, E.L. Pamo, E. Santofimia, O. Aduvire, J. Reyes, D. Barettino, Acid mine drainage in the Iberian Pyrite Belt (Odiel River watershed, Huelva, SW Spain): Geochemistry, mineralogy and environmental implications, Appl. Geochem. 20 (2005) 1320-1356.

416 [11] J.M. Nieto, A.M. Sarmiento, M. Olías, C.R. Canovas, I. Riba, J. Kalman, T.A.
417 Delvalls, Acid mine drainage pollution in the Tinto and Odiel rivers (Iberian
418 Pyritic Belt, SW Spain) and bioavailability of the transported metals to Huelva
419 Estuary, Environ. Int. 33 (2007) 445-455.

420 [12] A.M. Sarmiento, J.M. Nieto, C. Casiot, F. Elbaz-Poulichet, M. Egal, Inorganic
421 arsenic speciation at river basin scales: The Tinto and Odiel Rivers in the Iberian
422 Pyrite Belt, SW Spain, Environ. Pollut. 157 (2009) 1202-1209.

423 [13] K. Fukushi, M. Sasaki, T. Sato, N. Yanase, H. Amano, H. Ikeda, A natural
424 attenuation of arsenic in drainage from an abandoned arsenic mine dump, Appl.
425 Geochem. 18 (2003) 1267-1278.

426 [14] C. Casiot, M. Leblanc, O. Bruneel, J.C. Personne, K. Koffi, F.O. Elbaz-Poulichet,
427 Geochemical processes controlling the formation of As-rich waters within a
428 tailings impoundment (Carnoulès, France). Aquat. Geochem. 9 (2003) 273-290.

429 [15] A.G. Gault, D.R. Cooke, A.T. Townsend, J.M. Charnock, D.A. Polya, Mechanisms
430 of arsenic attenuation in acid mine drainage from Mount Bischoff, western
431 Tasmania, Sci. Total Environ. 345 (2005) 219-228.

432 [16] V. Oliveira, A.M. Sarmiento, J.L. Gómez-Ariza, J.M. Nieto, D. Sánchez-Rodas, New
433 preservation method for inorganic arsenic speciation in acid mine drainage
434 samples, Talanta 69 (2006) 1182-1189.

435 [17] T. To, K.D. Nordstrom, K. Cunningham, J. Ball, B. McCleskey, New method for the
436 direct determination of dissolved Fe(III) concentration in acid mine waters,
437 Environ. Sci. Technol. 33 (1999) 807-813.

438 [18] G.A. Waychunas, B.A. Rea, C.C. Fuller and J.A. Davis, Surface-chemistry of
439 ferrihydrite 1. EXAFS studies of the geometry of coprecipitated and adsorbed
440 arsenate, Geochim. Cosmochim. Acta 57 (1993) 2251-2269.

441 [19] S. Dixit, J.G. Hering, Comparison of arsenic (V) and arsenic (III) sorption onto iron
442 oxide minerals: Implications for arsenic mobility, Environ. Sci. Technol. 37 (2003)
443 4182-4189.

444 [20] M.P. Asta, C. Ayora, G. Román-Ross, J. Cama, P. Acero, A.G. Gault, J.M. Charnock,
445 F. Bardelli, Natural attenuation of arsenic in the Tinto Santa Rosa acid stream
446 (Iberian yritic Belt, SW Spain): the role of iron precipitates, Chem. Geol. (2009)
447 submitted.

448 [21] P.C. Singer, W. Stumm, Acidic mine drainage: the rate-limiting step, Science, 167
449 (1970) 1121-1123.

450 [22] R.B. McCleskey, D.K. Nordstrom, A.S. Maest, Preservation of water samples for
451 arsenic(III/V) determinations: an evaluation of the literature and new analytical
452 results, Appl. Geochem. 19 (2004) 995-1009.

453 [23] R.B. Johnston, P.C. Singer, Redox reactions in the Fe-As-O2 system, Chemosphere
454 69 (2007) 517-525.

455 [24] M.T. Emett, G.H. Khoe, Photochemical oxidation of arsenic by oxygen and iron in
456 acidic solutions, Water Research 35 (2001) 649-656.

457 [25] P. Acero, C. Ayora, C. Torrentó, J.M. Nieto, The role of trace elements during
458 schwertmannite precipitation and subsequent transformation into goethite and
459 jarosite, Geochim. Cosmochim. Acta 70 (2006) 4130-4139.

460 [26] J. Sánchez-España, E. López Pamo, E. Santofimia Pastor, The oxidation of ferrous
461 iron in acidic mine effluents from the Iberian Pyrite Belt (Odiel Basin, Huelva,
462 Spain): Field and laboratory rates, Journal of Geochemical Exploration 92 (2007)
463 120-132.

464 [27] U. Schwertmann, R.M. Cornell, Iron oxides in the Laboratory, New York., 1991.

465 [28] J.M. Bigham, U. Schwertmann, S.J. Traina, R.L. Windland, M. Wolf,
466 Schwermannite and the chemical modelling or iron in acid sulphate waters,
467 Geochim. Cosmochim. Acta 12 (1996) 2111-2121.

468 [29] J.Y. Yu, B. Heo, I.K. Choi, J.P. Cho, H.W. Chang, Apparent solubilities of
469 schwertmannite and ferrihydrite in natural stream waters polluted by mine
470 drainage, Geochim. Cosmochim. Acta 63 (1999) 3407-3416.

471 [30] K. Fukushi, T. Sato, N. Yanase, Solid-solution reactions in As(V) sorption by
472 schwertmannite, Environ. Sci. Technol. 37 (2003) 3581-3586.

473 [31] K. Fukushi, T. Sato, N. Yanase, J. Minato, H. Yamada, Arsenate sorption on
474 schwertmannite, Am. Mineral. 89 (2004) 1728-1734.

475 [32] D.L. Parkhurst, C.A.J. Appelo, User's Guide to PHREEQC (Version 2), a computer
476 program for speciation, batch reaction, one-dimensional transport, and inverse
477 geochemical calculations, Water Resources Research Investigations Report 99-4259,
478 1999, p. 312.

479 [33] J. Ball, D. Nordstrom, User's manual for WATEQ4F with revised thermodynamic
480 database and test cases for calculating speciation of major, trace and redox
481 elements in natural waters, U.S. Geological Survey Water-Resources Investigation
482 Report 91–183, 1991.

483 [34] P.C. Singer and W. Stumm, Kinetics of the oxidation of ferrous iron, 2nd Symp.
484 Coal Mine Drainage Res., Pittsburgh, Pennsylvania, 1968, pp. 12-34.

485 [35] D.M. McKnight, B.A. Kimball, K.E. Bencala, Iron photoreduction and oxidation in
486 an acidic mountain stream, Science 240 (4852) (1988) 637-640.

487 [36] D.M. McKnight, K.E. Bencala, Reactive iron transport in an acidic mountain stream
488 in Summit County, Colorado: A hydrologic perspective, Geochim. Cosmochim.
489 Acta 53 (1989) 2225-2234.

490 [37] A.M. Sarmiento, V. Oliveira, J.L. Gómez-Ariza, J.M. Nieto, D. Sánchez-Rodas, Diel
491 cycles of arsenic speciation due to photooxidation in acid mine drainage from the
492 Iberian Pyritic Belt (SW Spain), Chemosphere 66 (2007) 677-683.

493 [38] M.P. Asta, J. Cama, M. Martínez, J. Giménez, Arsenic removal by goethite and
494 jarosite in acidic conditions and its environmental implications, J. Hazard. Mater.
495 171 (2009) 965-972.

496

Titles of tables

Captions for figures

Figure 1. Site map and sampling points in the acid discharge of the Tinto Santa Rosa mine.

Figure 2. Comparison between simulated and measured data of concentration of Fe(II), Fe(III) and total iron (a,b), and of pH (c,d) from the Tinto Santa Rosa stream. Error bars correspond to the analytical error (10% for Fe(II) and Fe(III), 3% for total iron and 0.05 for pH). First data correspond to the TS1-TS2 mixing point.

Figure 3. Comparison between simulated and measured data for As(III) and As(V) concentrations in the Tinto Santa Rosa stream. Error bars correspond to the analytical error (15%). The first data correspond to the TS1-TS2 mixing point.

Figure 4. Simulated pH evolution for different rate constants of Fe(II) oxidation compared with measured data from the March 2008 campaign (except the first datum, which corresponds to the TS1-TS2 mixing point). Error bars correspond to the pH measurement error, which is ±0.05 pH units.

Figure 5. Simulated evolution of Fe(II) (a) and Fe(III) (b) concentrations (mol L^{-1}) for different rate constants of Fe(II) oxidation compared with measured data from the March 2008 campaign (except the first data, which correspond to the TS1-TS2 mixing point). Error bars in concentrations correspond to the analytical error of 10%.

Figure 6. Simulated evolution of As(III) and As(V) concentrations (mol L^{-1}) for different rate constants of arsenite oxidation compared with measured data from the March 2008 campaign (except the first data, which correspond to the TS1-TS2 mixing point) Error bars in concentrations correspond to the analytical error of 15 %.

Figure 7. Simulated evolution of pH (a) and Fe(III) concentration (mol L^{-1}) (b) for different rate constants of schwertmannite precipitation compared with measured data from the March 2008 campaign (except the first data, which correspond to the TS1-TS2 mixing point). Error bars correspond to the analytical error (10% for Fe(III) and 0.05 for pH).

Figure 8. Simulated evolution of As(V) concentrations (mol L^{-1}) using different distribution coefficients (including that of Fukushi et al. [30]) compared with measured data from the March 2008 campaign (except the first datum, which corresponds to the TS1-TS2 mixing point). Error bars in concentrations correspond to the analytical error of 15 % for As(V).

Table 1

Click here to download high resolution image

	Sample (filtered)	T (°C)	pH	Eh (mV)	Conductivity (μS cm^{-1})	mg L^{-1}												μg L^{-1}									
						Ca	Mg	Na	K	Al	SO_4	Fe TOT	Fe(III)	Fe (II)	Mn	Si	Zn	Cu	As TOT	As(V)	As(III)	Pb	Ni	Sb	Ti	V	Cd	Co
February 2008	TS1	18.9	3.49	561.5	3750	167	133	26.54	2	83	2893	749	165	584	38	37	69	17	1956	1348	608	1	490	*bdl*	4	55	82	858
	TS2	18.7	3.53	510.5	3200	169	135	26.85	2	81	2853	726	162	564	39	37	68	15	2382	1362	1020	387	493	4.1	4	55	82	855
	TS3	18.1	3.41	598.5	2620	171	136	26.75	1	84	2861	722	188	534	39	38	69	17	1351	962	389	129	492	*bdl*	3	30	84	855
	TS4	15.3	3.37	603.5	2890	171	136	26.51	1	84	2885	708	185	523	39	38	69	17	1412	1064	348	127	486	*bdl*	3	33	84	862
	TS5	19.1	3.26	613.5	2480	172	138	27.14	1	86	2876	683	195	488	39	39	70	17	1145	855	290	127	512	*bdl*	3	25	86	886
	TS6	15.2	3.27	620.5	3150	171	135	26.32	1	84	2866	664	204	460	38	38	68	17	1064	783	281	118	490	*bdl*	3	24	83	847
	TS7	12.5	3.25	624.5	3030	172	136	26.48	2	85	2899	666	213	453	39	39	70	17	991	706	285	118	502	*bdl*	3	23	84	863
	TS8	14.9	3.16	634.5	2580	170	136	26.84	2	86	2865	645	238	407	39	38	69	17	863	656	207	113	487	*bdl*	3	20	82	836
March 2007[a]	TS1	15.1	2.93	580.7	3490	187	153	26	5	116	3623	845	187	658	45	37	83	46	1365	1349	16	1	904	4	54	102	146	1306
	TS2	18.5	2.97	546.1	3220	172	138	26	4	97	3024	694	151	543	39	34	68	33	2731	1763	968	654	754	24	42	74	118	1078
	TS3	12	2.95	614.5	3270	194	157	27	4	118	3563	779	247	532	45	40	80	43	1401	1196	205	211	836	7	46	70	135	1184
	TS4	13.4	2.81	617.5	3150	183	149	26	4	112	3353	719	313	406	43	39	76	41	1384	1271	113	214	895	7	49	70	146	1277
	TS5	12.9	2.78	627.5	4050	195	159	27	4	119	3563	759	427	332	46	41	82	44	1149	1119	29	196	827	5	42	53	130	1170
	TS6	13.3	2.76	632.5	3900	188	154	26	3	115	3503	717	340	377	44	41	80	42	1155	1128	27	202	869	5	47	54	139	1243
	TS7	12.6	2.79	635.5	3040	190	155	27	3	116	3443	711	347	364	44	41	79	42	948	948	*bdl*	175	777	3	40	42	123	1104
	TS8	13.2	2.67	643.5	3020	193	159	27	2	118	3563	708	372	336	45	42	81	43	953	953	*bdl*	191	856	3	48	43	137	1214

bdl: below detection limit

[a] Data from Asta et al. [20]

Table 2

Click here to download high resolution image

Sample	Water sample	Major oxides (wt %)								Trace metals (mg kg^{-1})										
		Na_2O	MgO	Al_2O_3	SO_3	K_2O	CaO	Fe_2O_3	As_2O_3	Cu	Mn	Zn	As	Cd	Ni	Sb	V	Pb	Co	Sr
TSR-M-1	**TS1**	0.03	0.02	9.55	8.92	0.01	0.05	83.76	6.64	192	70	118	34200	*bdl*	*bdl*	14	397	*bdl*	2	2
TSR-M-2	**TS7**	*bdl*	0.38	12.28	12.94	0.02	0.58	84.68	0.24	840	1120	1496	1176	72	64	2	84	92	26	5
TSR-M-3	**TS8**	*bdl*	0.09	*bdl*	9.96	0.01	0.14	76.70	0.16	2816	420	400	756	72	36	2	64	100	4	2
TSR-M-4	**TS3**	0.26	0.16	7.26	6.59	2.30	0.09	77.29	1.19	618	127	129	4829	bdl	11	136	184	5743	3	27
TSR-M-5	**TS6**	0.25	0.11	7.74	8.16	1.39	0.07	82.57	0.81	1176	115	602	3616	15	5	27	69	6535	3	23
TSR-M-6	**TS7**	0.26	0.16	1.26	7.82	1.63	0.14	81.55	0.33	332	400	180	1436	52	16	39	136	1204	4	27
TSR-M-7-(0-3.5 cm)	**TS1**	0.02	0.03	0.20	9.03	0.08	0.33	88.42	1.69	332	584	248	11280	100	44	17	640	196	28	1
TSR-M-7-(3.5-5.5 cm)		*bdl*	*bdl*	*bdl*	8.40	0.10	0.05	87.49	3.71	140	460	128	22040	72	*bdl*	26	820	128	2	2
TSR-M-8-(0-0.5 cm)	**TS3**	*bdl*	0.01	1.40	8.25	0.17	0.22	88.03	2.37	168	476	148	14240	70	*bdl*	9	220	372	1	4
TSR-M-8-(0.5-4 cm)		*bdl*	*bdl*	0.72	9.73	0.31	0.05	86.12	2.02	168	360	132	9880	72	12	71	320	352	2	6
TSR-M-8-(4-4.5 cm)		*bdl*	0.01	0.38	8.32	0.07	0.08	88.85	2.11	220	572	220	14320	100	16	21	320	256	7	3
TSR-M-8-(4.5-7 cm)		*bdl*	0.05	0.00	8.50	0.10	0.13	89.10	1.58	340	528	368	8320	112	*bdl*	7	220	264	5	3
TSR-M-9-(0-5 cm)	**TS6**	*bdl*	0.03	1.18	8.82	0.26	0.09	88.97	0.52	200	456	160	2784	88	16	15	180	480	2	5
TSR-M-9-(5-10 cm)		*bdl*	0.02	*bdl*	7.79	0.25	0.12	89.98	0.65	280	472	180	3628	80	*bdl*	8	148	448	2	5
TSR-M-10-(0-2 cm)	**TS8**	*bdl*	0.01	0.27	8.93	0.17	0.10	89.42	0.53	140	48	180	3236	92	*bdl*	8	136	332	2	4
TSR-M-10-(2-4.5 cm)		0.61	bdl	2.26	7.43	0.09	0.11	90.90	0.48	180	404	168	2340	64	*bdl*	3	96	28	2	3
TSR-M-10-(4.5-7 cm)		*bdl*	0.01	*bdl*	4.57	0.08	0.04	93.86	0.32	220	1056	1500	3340	200	*bdl*	10	160	352	14	7

bdl: below detection limit

Numbers in brackets "( )" indicate the depth below the precipitate-water interface

Table 3

Click here to download high resolution image

Equation	Reaction	Rate expression (mol $L^{-1} s^{-1}$)	Model rate constant		Reported and calculated rate constant values	
	Fe(II) oxidation		Mar-07	Feb-08		
(1)	$Fe^{2+} + 0.25 O_2(aq) + H^+ = Fe^{3+} + 0.5 H_2O$	$r_{Fe(II)} = \frac{-d[Fe(II)]}{dt} = k_{Fe}[Fe(II)]\, f_{O2}$	$10^{-3.55}$	$10^{-3.75}$	$10^{-3.43}$ $10^{-3.47}$ $10^{-3.9}$ - $10^{-5.2}$	(1) (2) (3)
	As(III) oxidation (a)					
(2)	$2Fe^{3+} + H_3AsO_3 + H_2O + h\nu = 2Fe^{2+} + H_3AsO_4 + 2H^+$	$r_{As(III)} = \frac{-d[As(III)]}{dt} = k_{As}[As(III)][Fe(III)]$	$10^{-1.20}$	$10^{-1.20}$	$10^{-2.2}$ - $10^{-2.8}$	(3)
	Schwertmannite precipitation (b)					
(3)	$8Fe^{3+} + 2.07SO_4^{2-} + 11.86H_2O = Fe_8O_8(SO_4)_{1.07}(OH)_{13.86} + 19.86H^+$	$r_{Sch} = k_{Sch}[Fe(III)][H^+]^{-1}$	$10^{-8.0}$	$10^{-8.5}$	$10^{-8.10}$	(4)
	As(V) sorption (c)					
(4)	$Schwertmannite + H_3AsO_4 + 0.24OH^- = As\text{-}Schw + 0.62\, SO_4^{2-} + 0.24\, H_2O + H^+$	$r_{As(V)} = r_{Sch}\, k_d\, [As(V)]$	$10^{3.42}$	$10^{3.90}$	$10^{4.5}$ - $10^{5.0}$	(5)

"h ν" is photons

(a) Reaction proposed by Emett and Khoe [24]

(b) Calculated schwertmannite composition of Tinto Santa Rosa acid discharge

(c) Reaction proposed by Fukushi et al. [30]

Ω = saturation index

K_d = distribution coefficient

(1) fO_2 of $10^{-0.67}$ was included in the rate constant reported by McKnight and Bencala [36]

(2) fO_2 of $10^{-0.67}$ was included in the rate constant reported by McKnight et al. [35]

(3) Rate constant values obtained under laboratory conditions (unpublished data)

(4) Calculated modelling the data of Acero et al. [25]

(5) Calculated from the data of Fukushi et al. [30]

Figure 1

Click here to download high resolution image

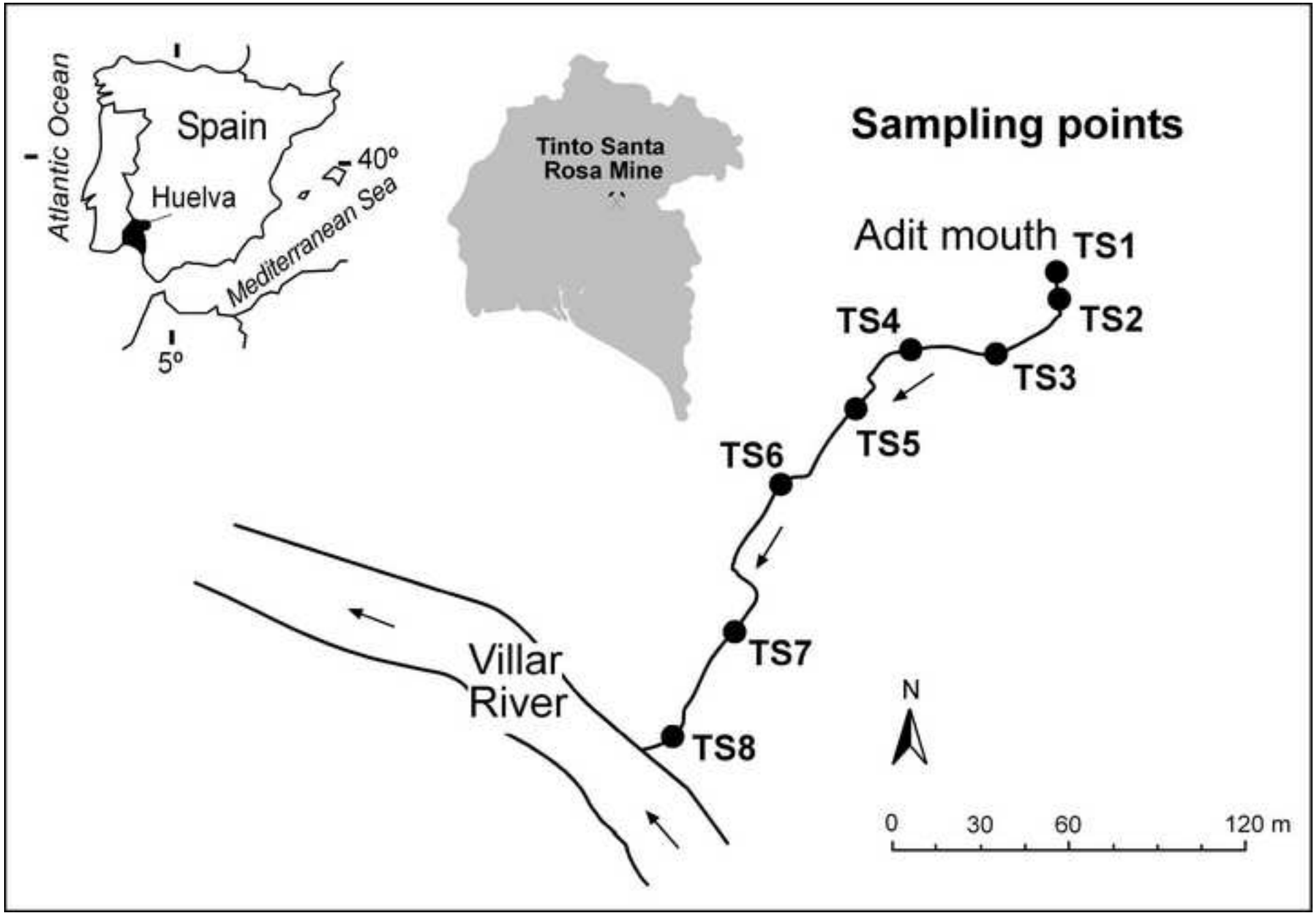

Figure 2a

Click here to download high resolution image

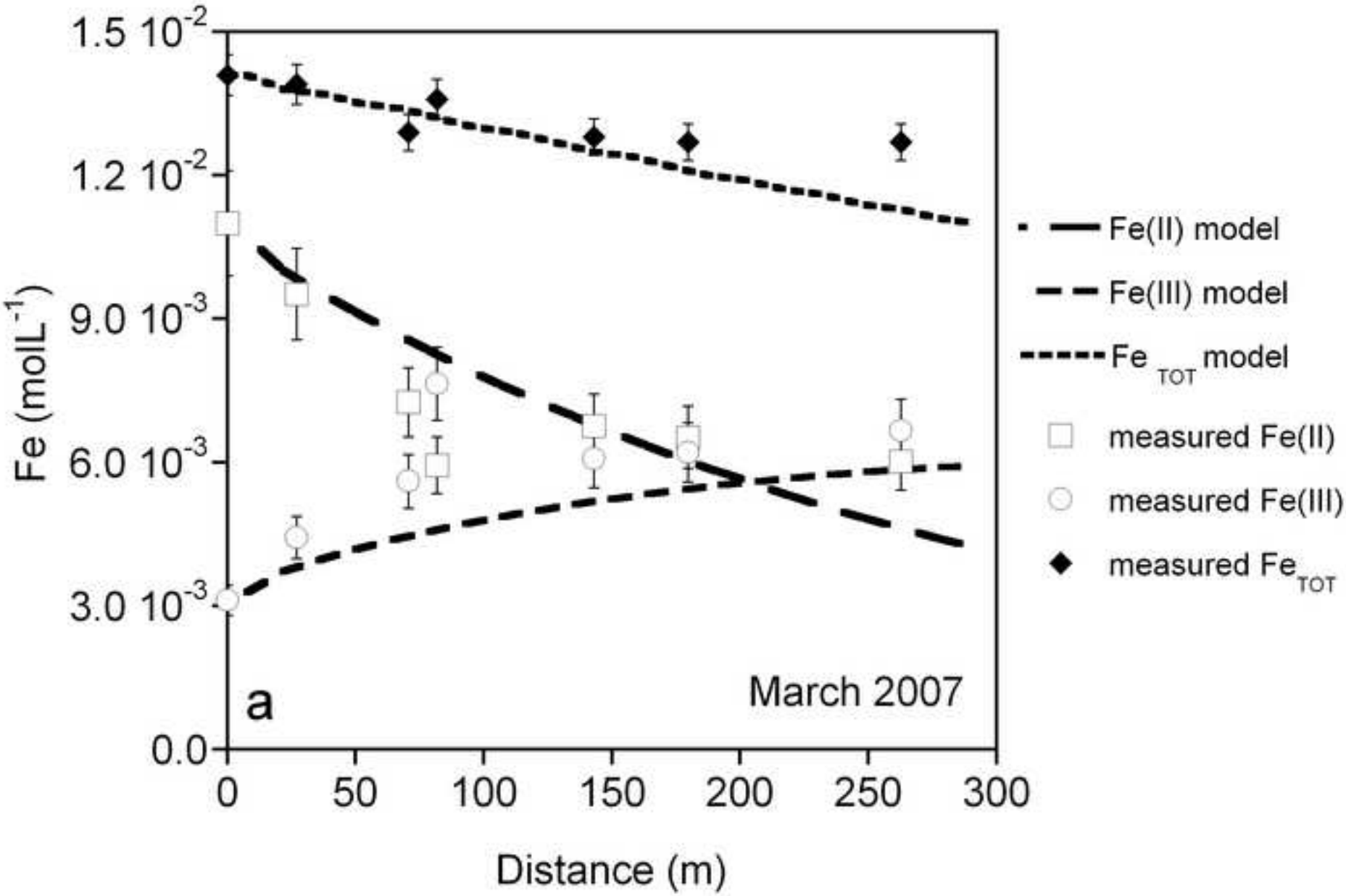

Figure 2b

Click here to download high resolution image

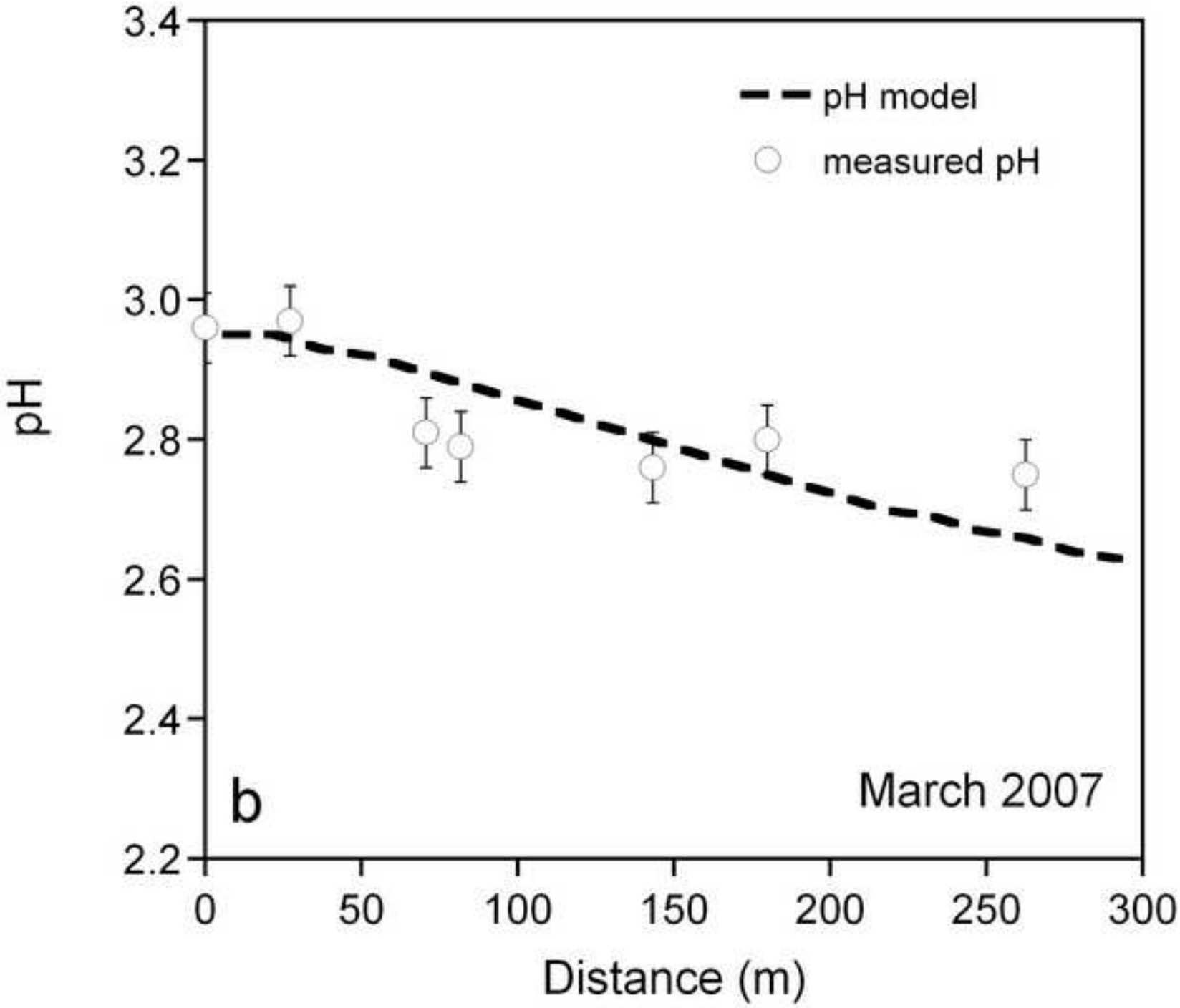

Figure 2c

Click here to download high resolution image

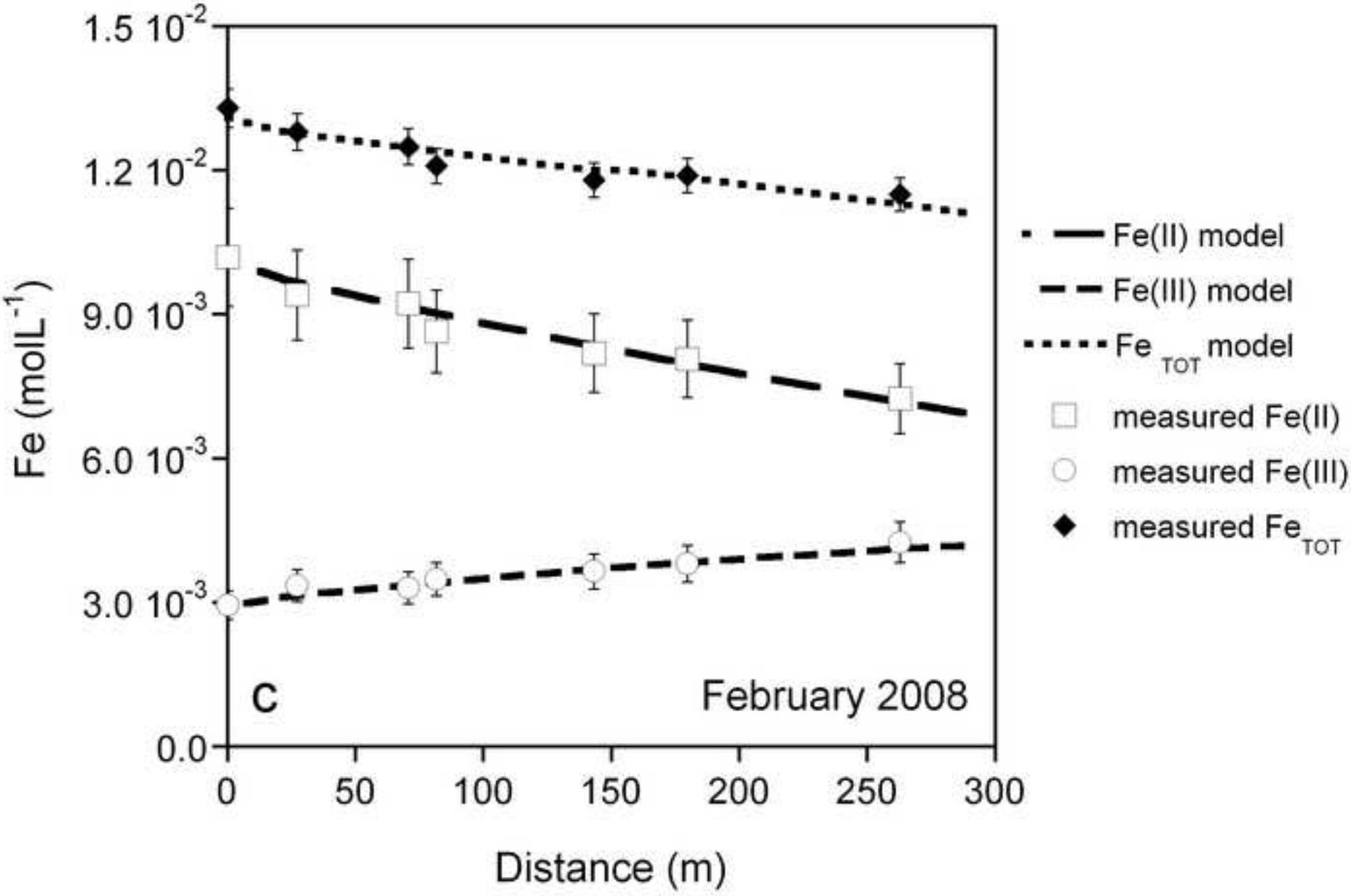

Figure 2d

Click here to download high resolution image

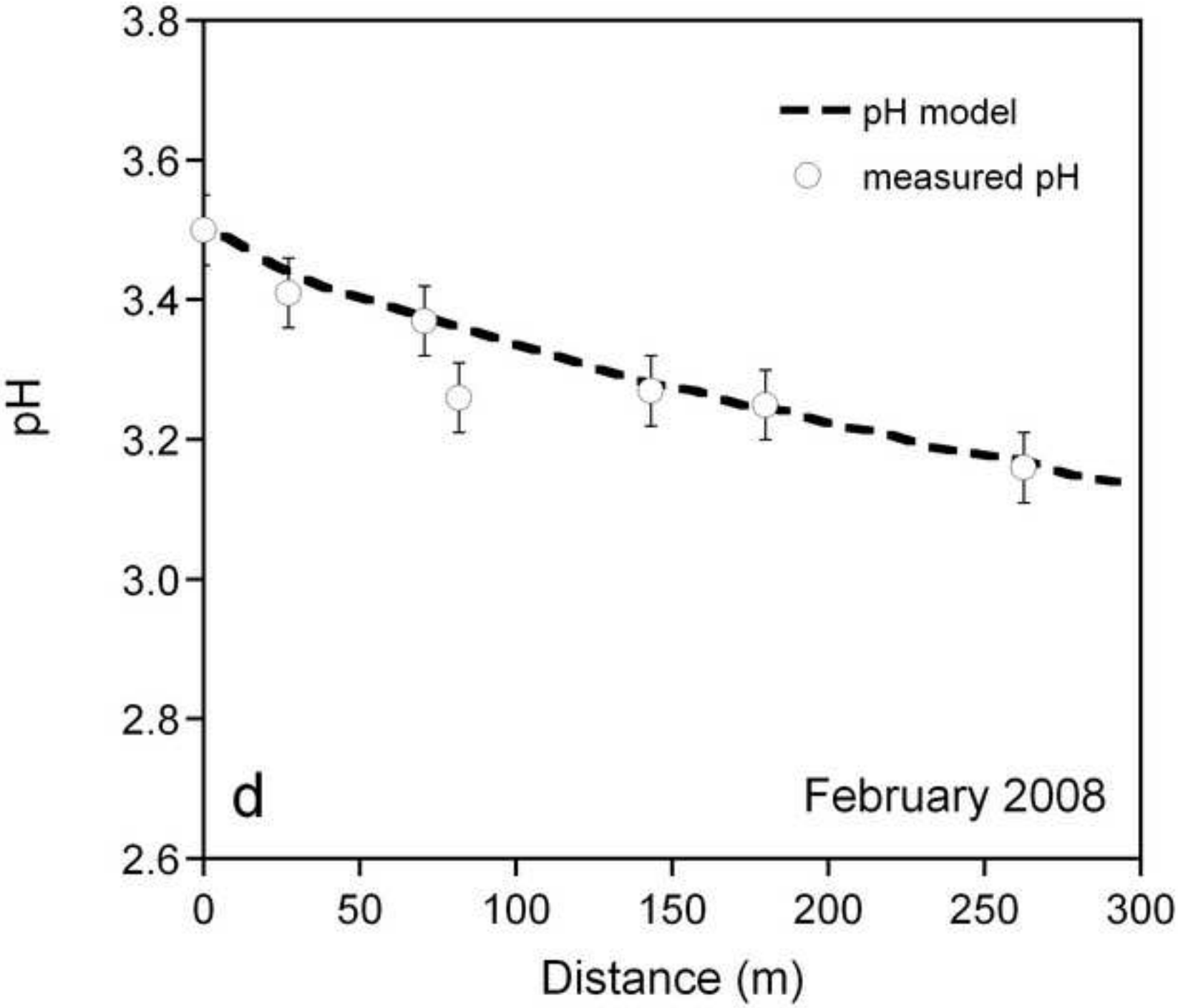

Figure 3a

Click here to download high resolution image

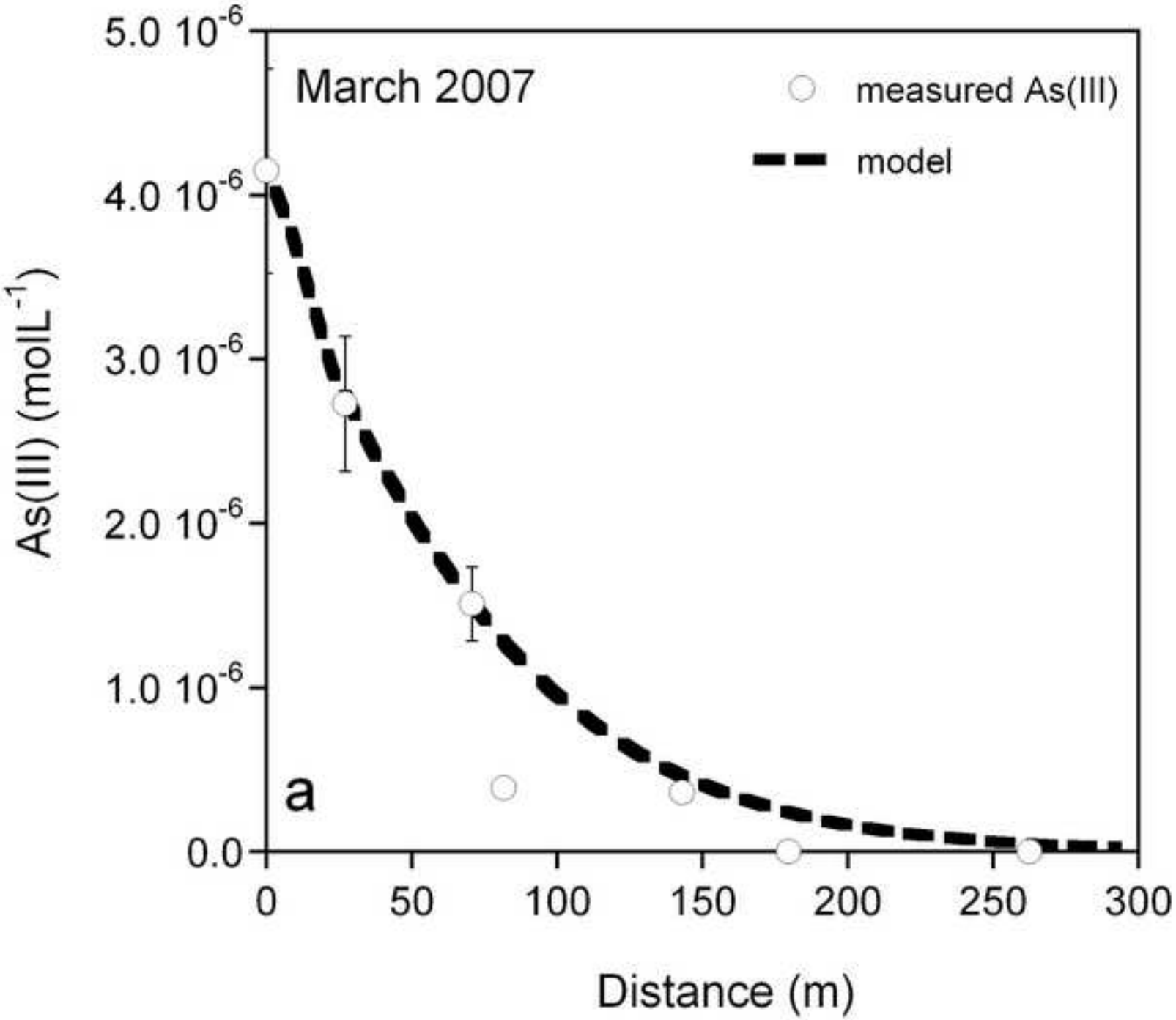

Figure 3b
Click here to download high resolution image

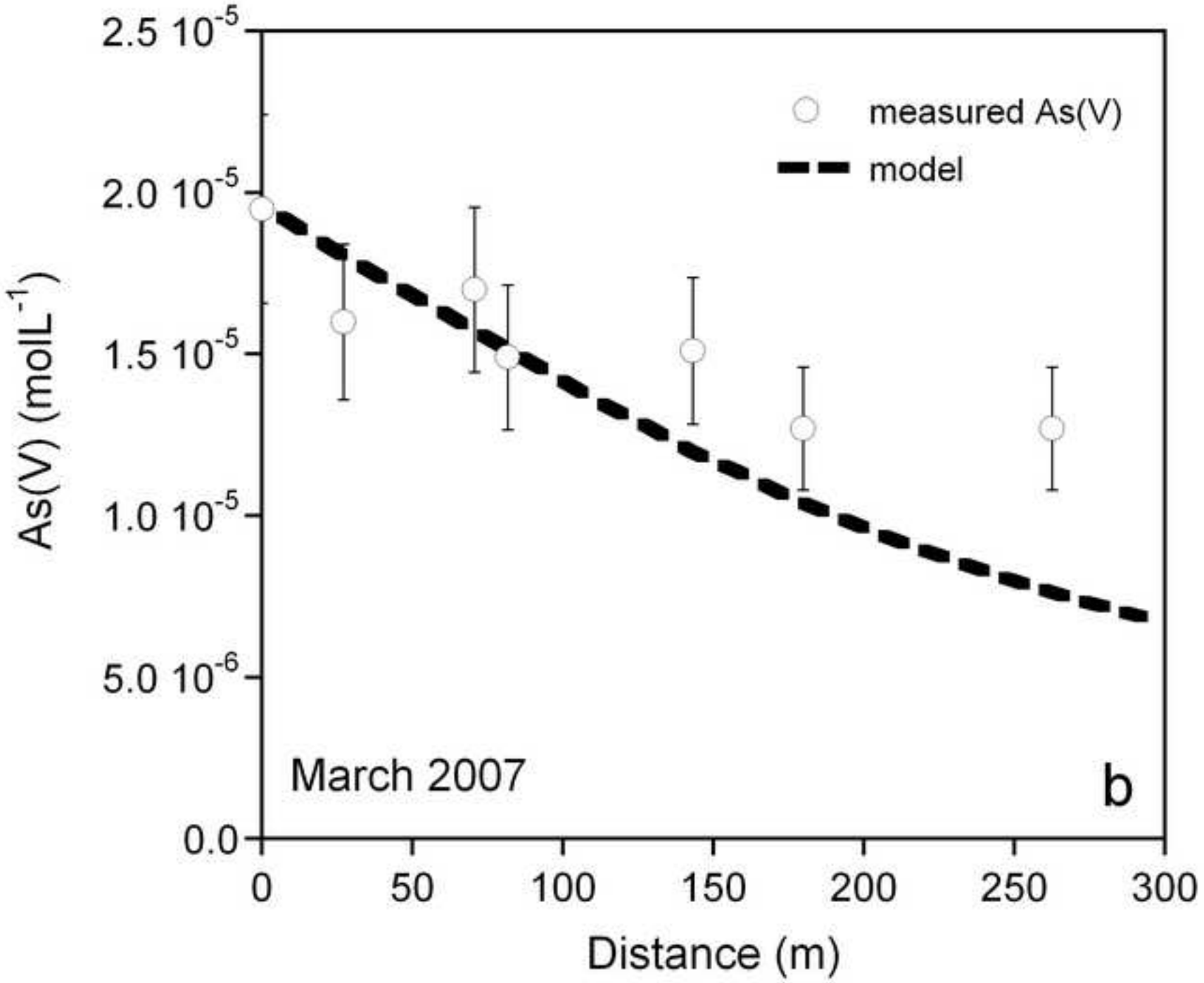

Figure 3c

Click here to download high resolution image

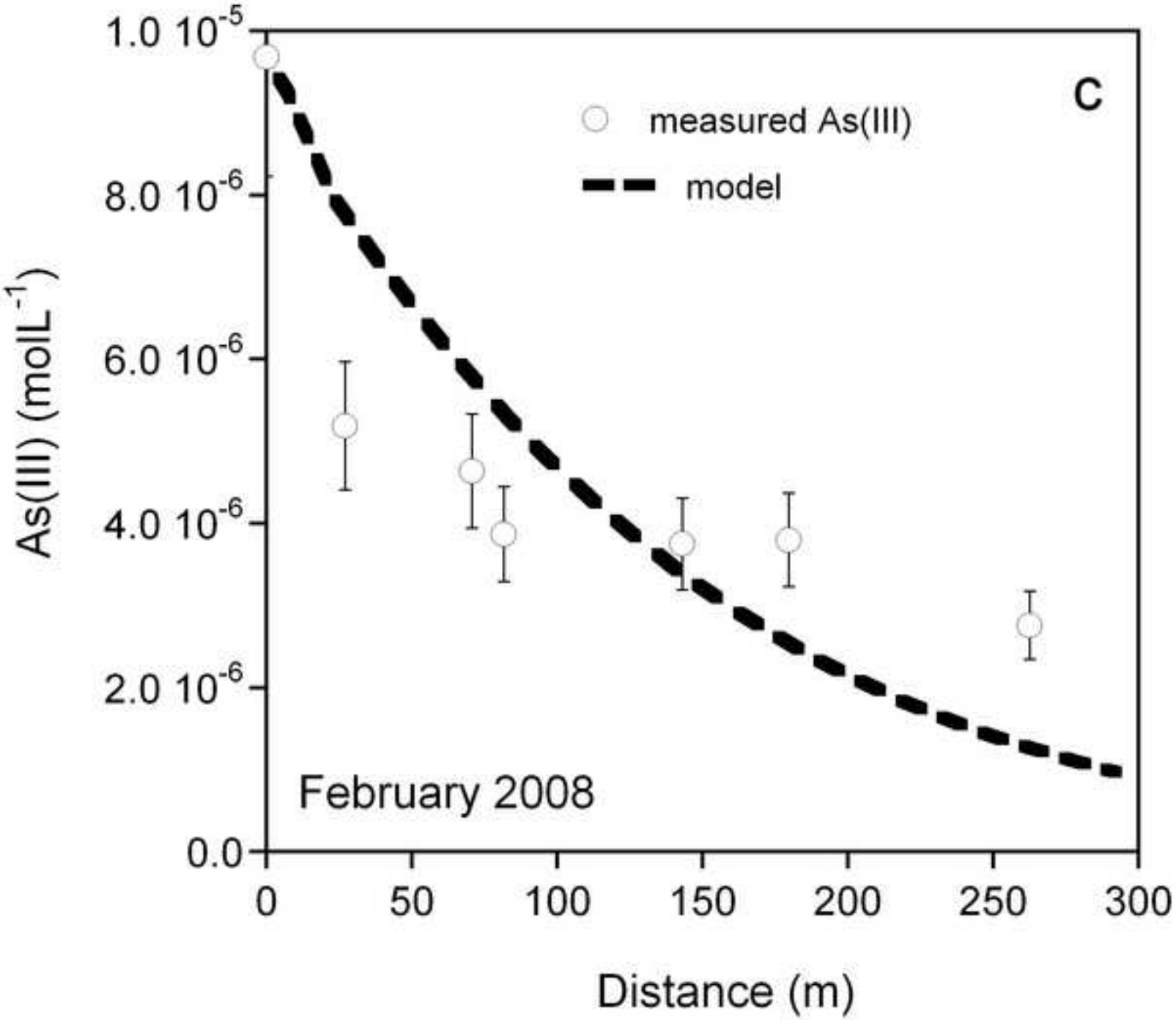

Figure 3d
Click here to download high resolution image

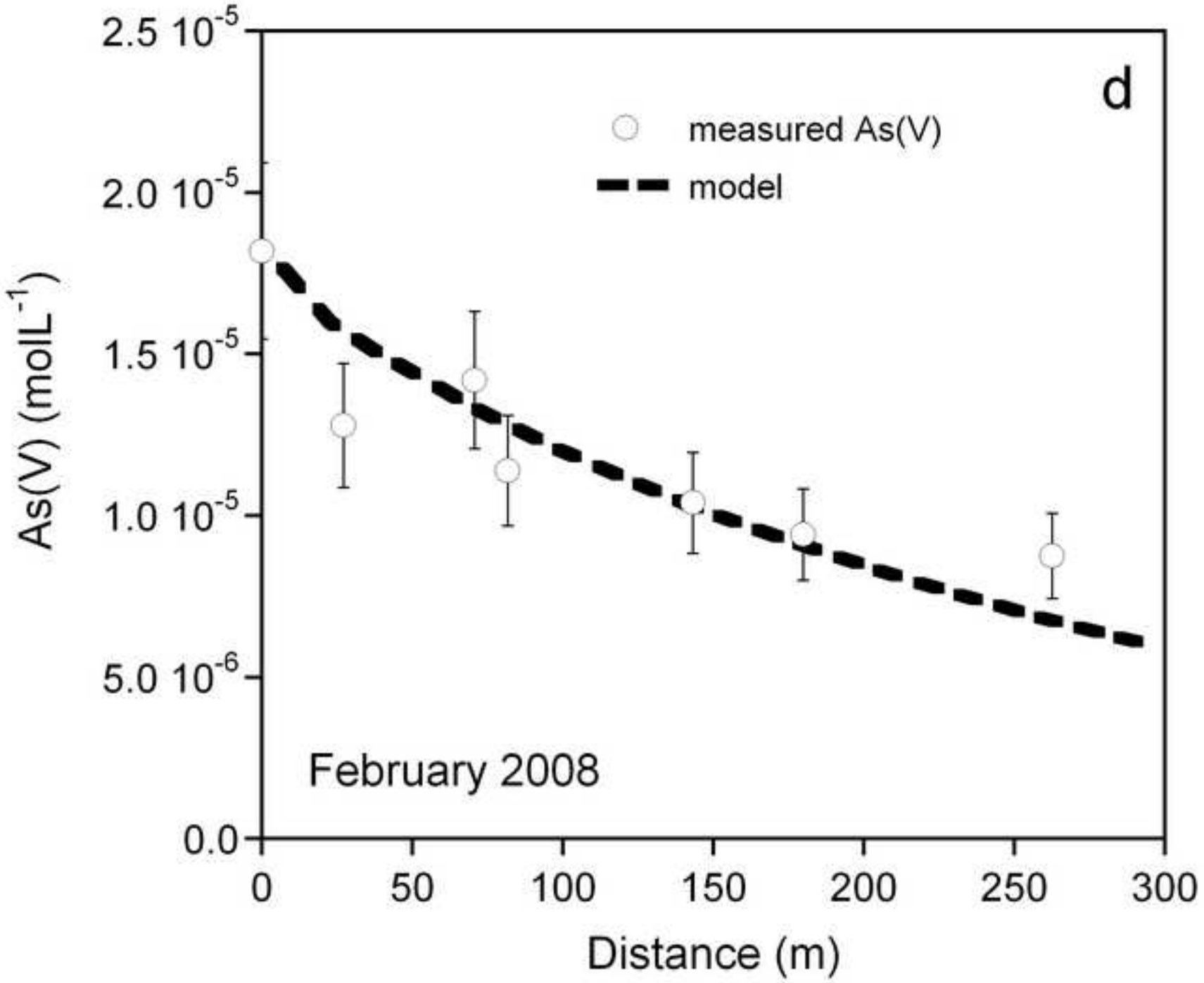

Figure 4

Click here to download high resolution image

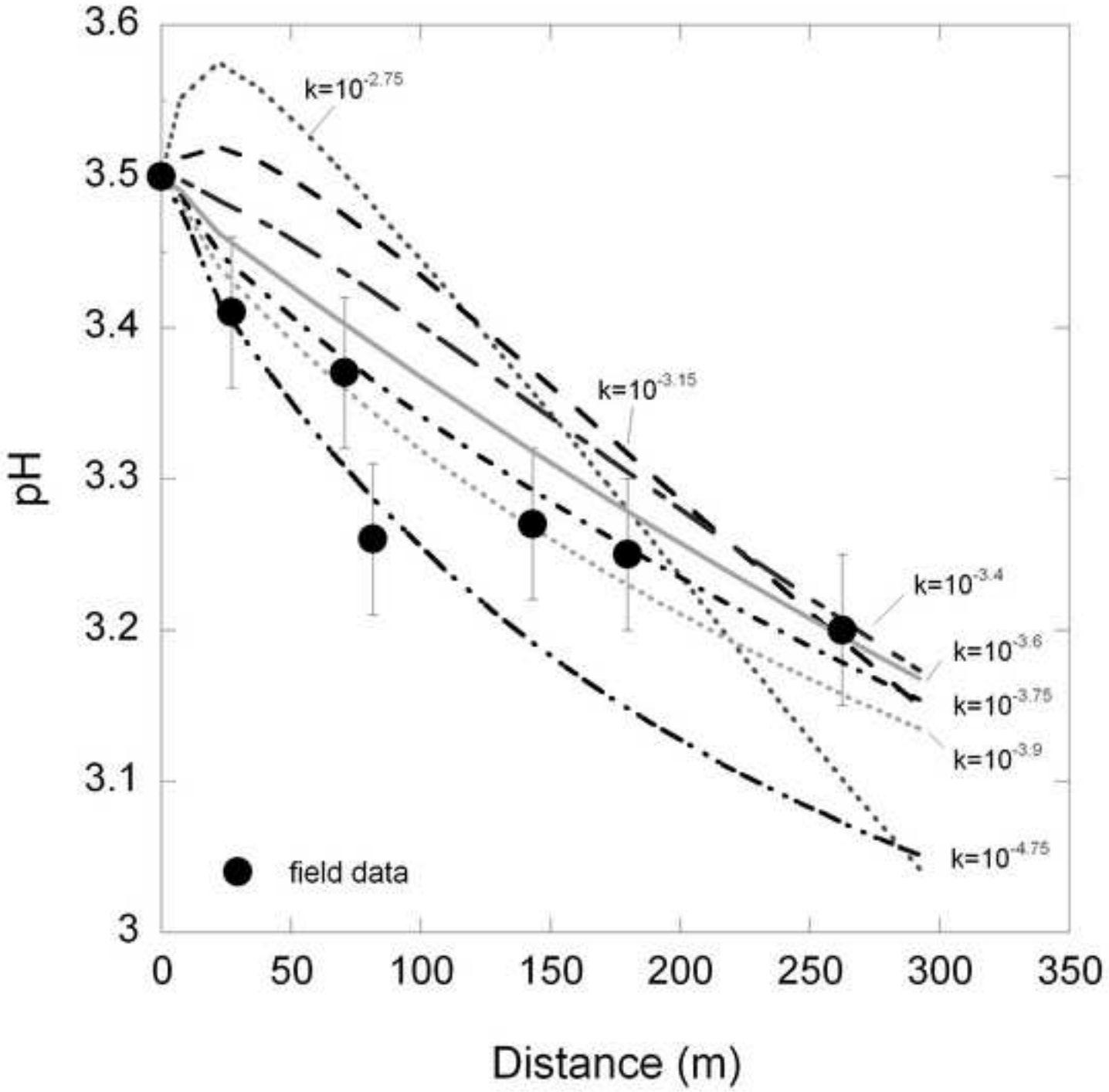

Figure 5a

Click here to download high resolution image

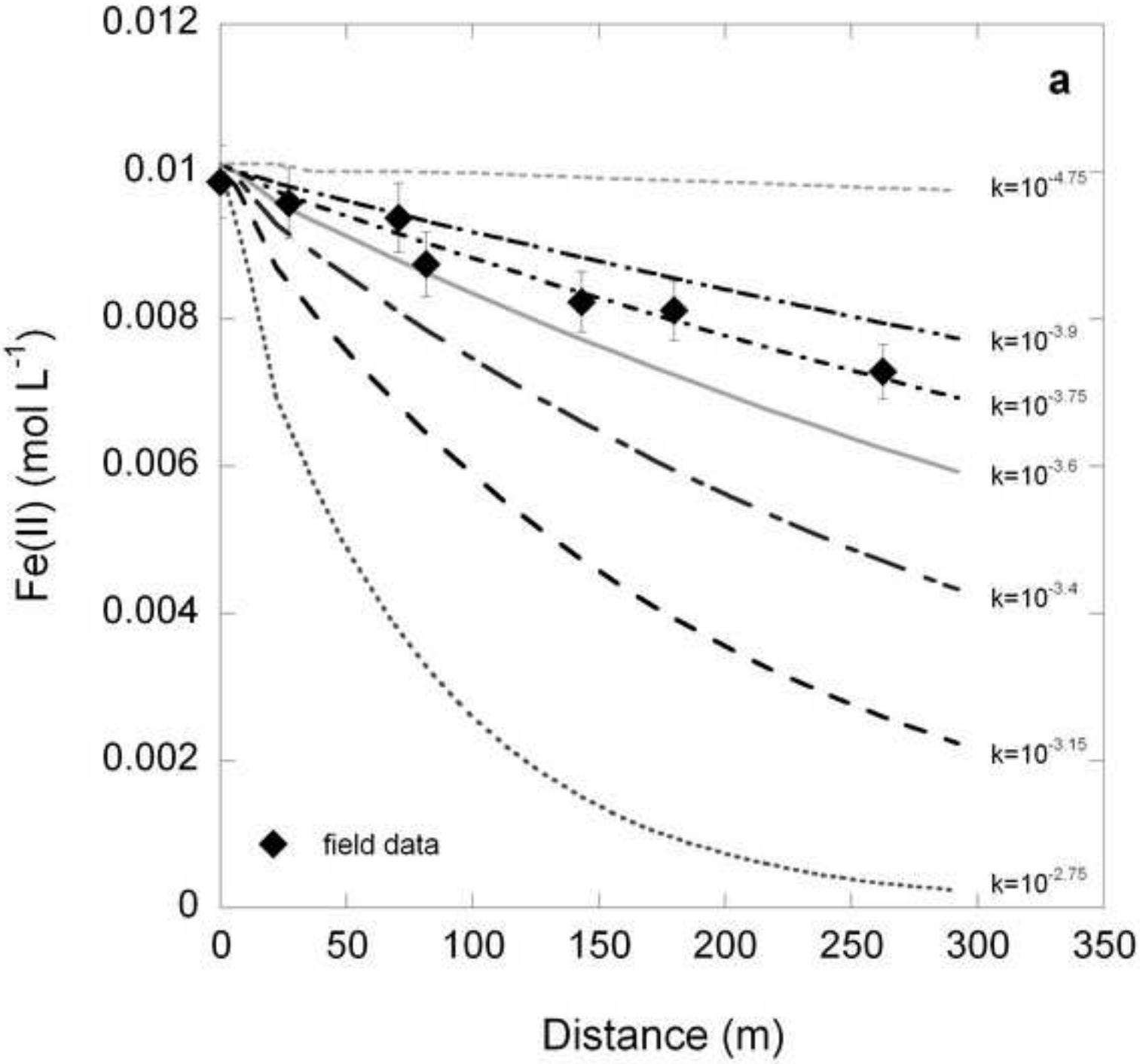

Figure 5b

Click here to download high resolution image

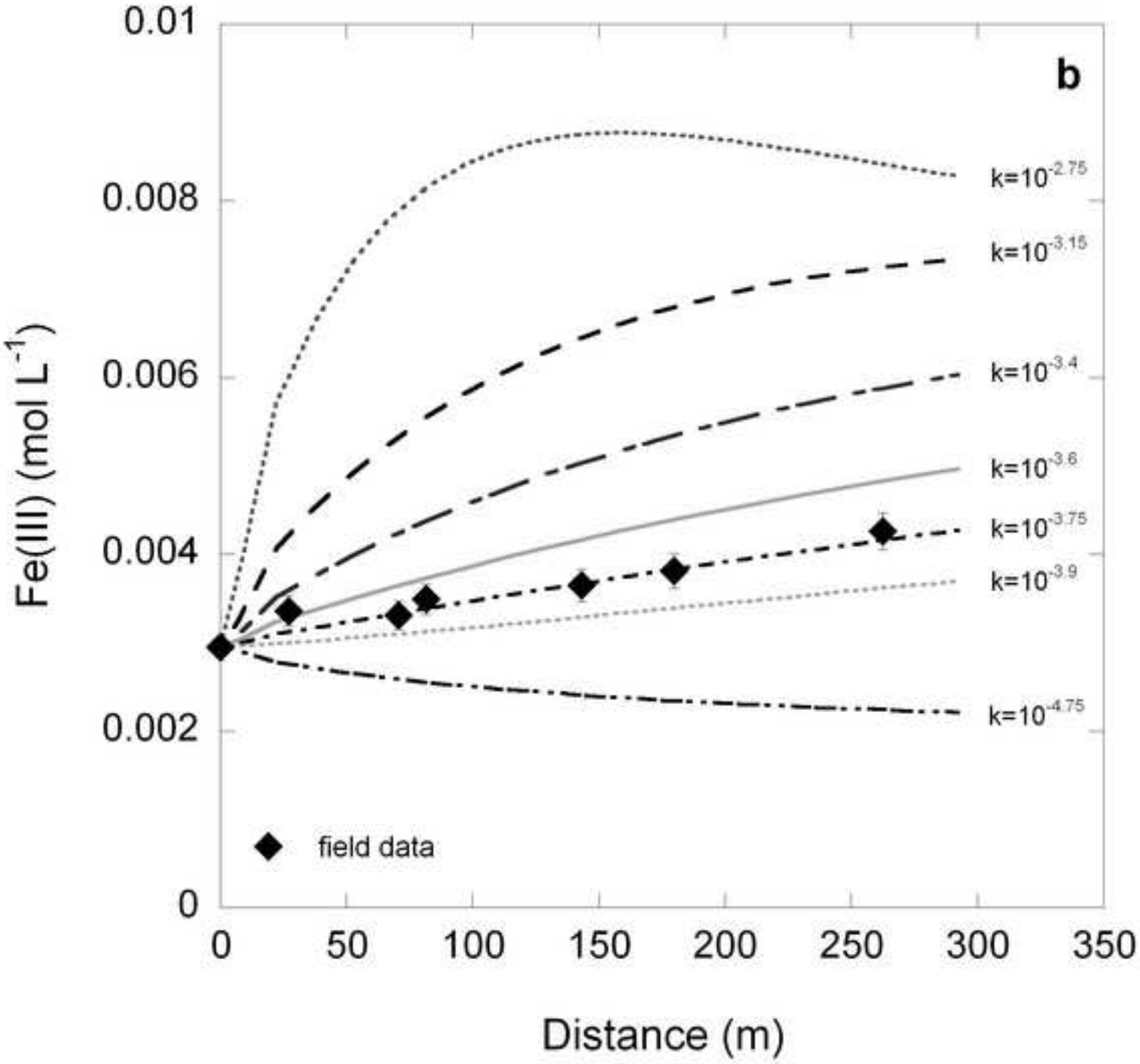

Figure 6a

Click here to download high resolution image

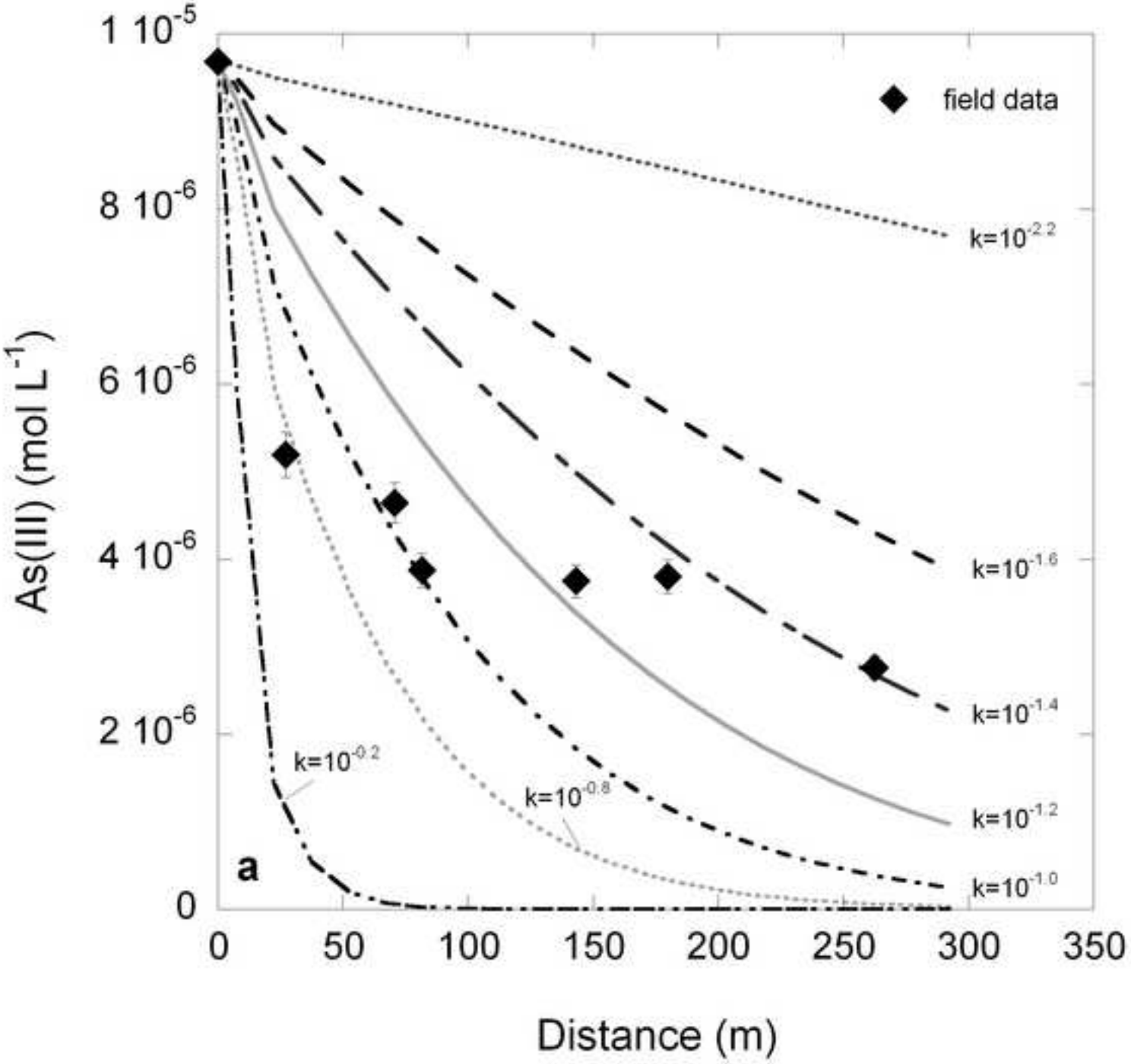

Figure 6b

Click here to download high resolution image

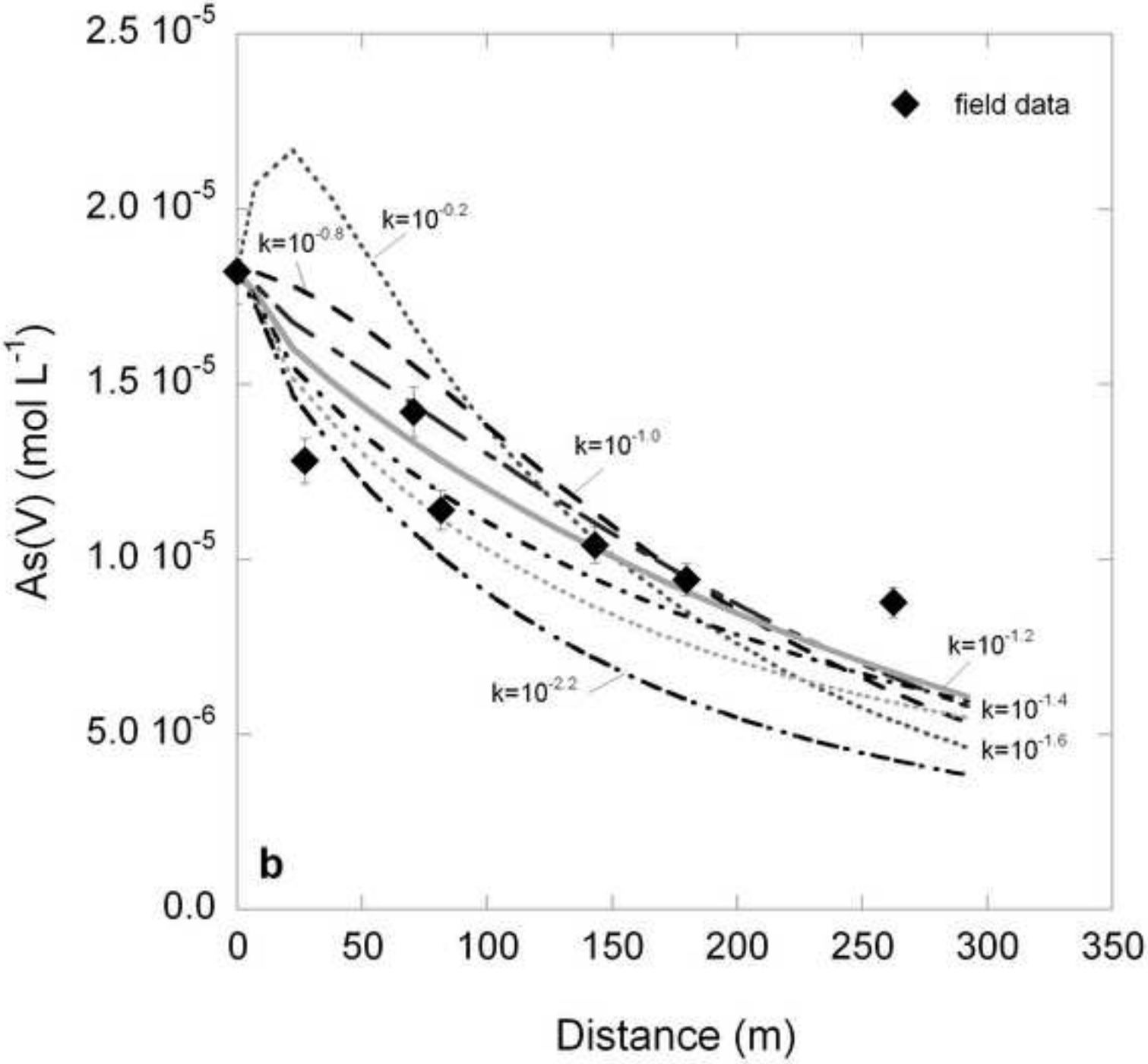

Figure 7a

Click here to download high resolution image

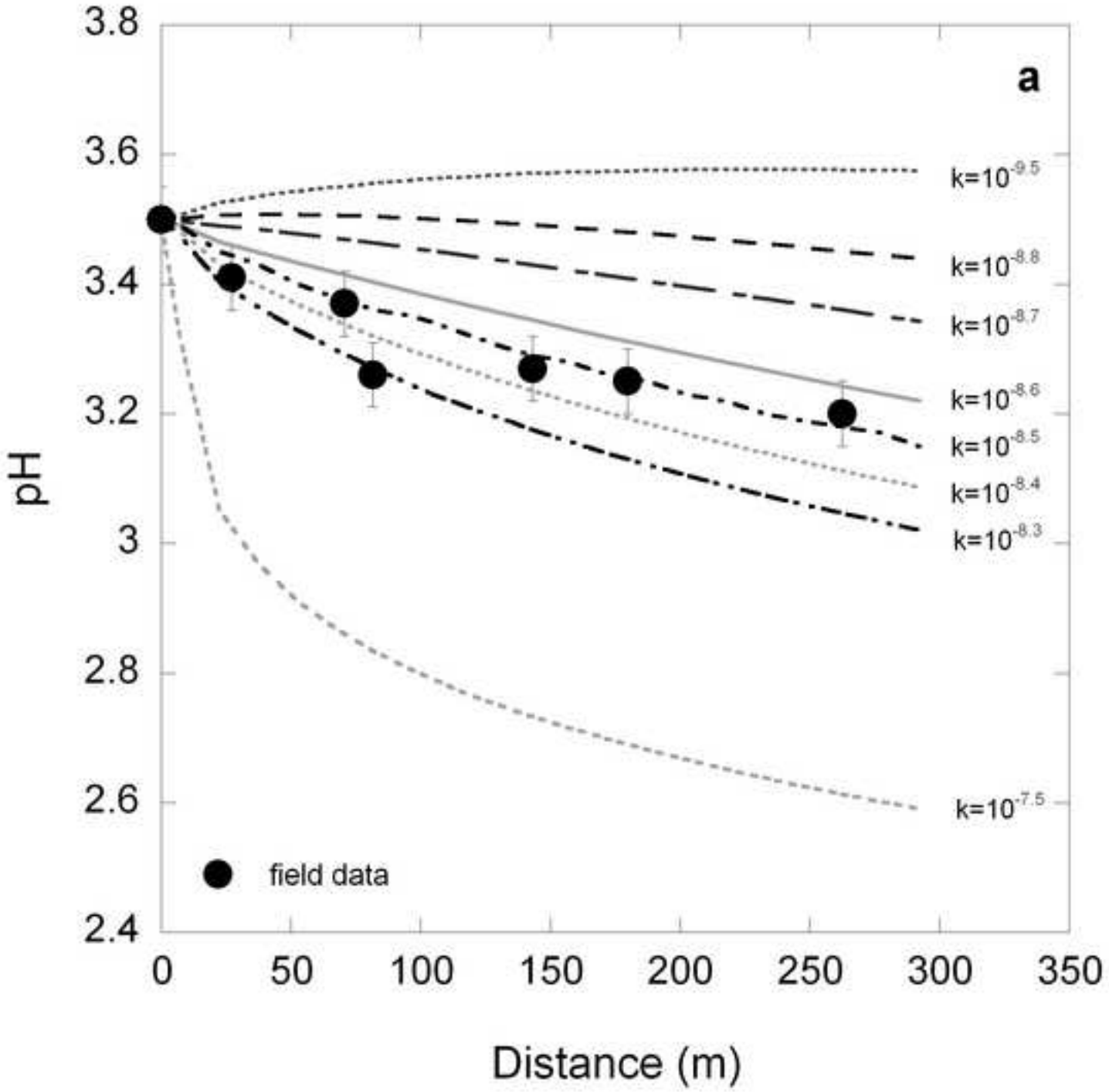

Figure 7b

Click here to download high resolution image

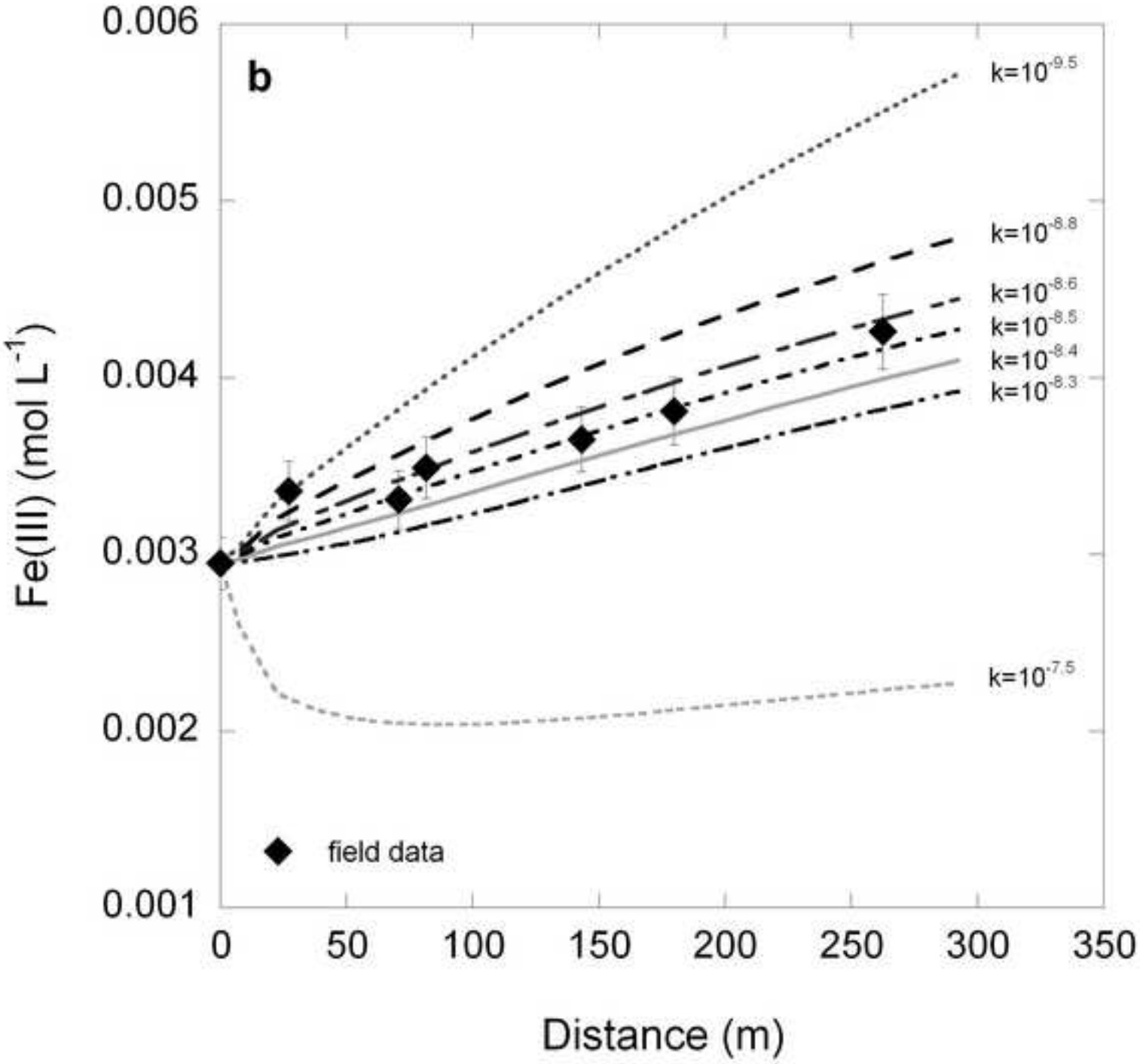

Figure 8

Click here to download high resolution image